Tectonic evolution of the Pamir recorded in the western Tarim Basin (China): sedimentologic and magnetostratigraphic analyses of the Aertashi section

Tasmin Blaynay, Guillaume Dupont-Nivet, Yani Najman, Jean-Noël Proust, Nils Meijer, Pierrick Roperch, Edward R Sobel, Ian Miller, Zhajie Guo

Tectonics

RESEARCH ARTICLE
10.1029/2018TC005146

Key Points:
- ~41 Ma, retreat of the Tarim Sea coincides with tectonic subsidence attributed to the effects of uplift of the Tibetan plateau to the south
- From 24.3–21.6 Ma a depositional hiatus followed by fining upward conglomeratic deposition is attributed to fault propagation into the Tarim
- At 15.0 Ma, Pamir sourced material, a shift to EW compression and clockwise vertical-axis rotation indicates the Pamir had reached Aertashi

Supporting Information:
- Supporting Information S1
- Table S1
- Table S2
- Data Set S1

Correspondence to:
T. Blayney,
t.a.blayney@hotmail.co.uk

Citation:
Blayney, T., Dupont-Nivet, G., Najman, Y., Proust, J.-N., Meijer, N., Roperch, P., et al. (2019). Tectonic evolution of the Pamir recorded in the western Tarim basin (China): Sedimentologic and magnetostratigraphic analyses of the Aertashi section. *Tectonics*, *38*, 492–515. https://doi.org/10.1029/2018TC005146

Received 15 MAY 2018
Accepted 22 DEC 2018
Accepted article online 8 JAN 2019
Published online 8 FEB 2019

Tectonic Evolution of the Pamir Recorded in the Western Tarim Basin (China): Sedimentologic and Magnetostratigraphic Analyses of the Aertashi Section

Tamsin Blayney[1], Guillaume Dupont-Nivet[2,3,4], Yani Najman[1], Jean-Noël Proust[2], Niels Meijer[3], Pierrick Roperch[2], Edward R. Sobel[3], Ian Millar[5], and Zhaojie Guo[4]

[1]Lancaster Environment Centre, Lancaster University, Bailrigg, UK, [2]Université Rennes, CNRS, Géosciences Rennes - UMR, Rennes, France, [3]Institute for Earth and Environmental Science, Potsdam University, Potsdam, Germany, [4]Key Laboratory of Orogenic Belts and Crustal Evolution, Ministry of Education, Beijing, China, [5]NERC Isotope Geosciences Laboratory, BGS Keyworth, Nottingham, UK

Abstract The northward indentation of the Pamir salient into the Tarim basin at the western syntaxis of the India-Asia collision zone is the focus of controversial models linking lithospheric to surface and atmospheric processes. Here we report on tectonic events recorded in the most complete and best-dated sedimentary sequences from the western Tarim basin flanking the eastern Pamir (the Aertashi section), based on sedimentologic, provenance, and magnetostratigraphic analyses. Increased tectonic subsidence and a shift from marine to continental fluvio-deltaic deposition at 41 Ma indicate that far-field deformation from the south started to affect the Tarim region. A sediment accumulation hiatus from 24.3 to 21.6 Ma followed by deposition of proximal conglomerates is linked to fault propagation into the Tarim basin. From 21.6 to 15.0 Ma, increasing accumulation rates of fining upward clastics is interpreted as the expression of a major dextral transtensional system linking the Kunlun to the Tian Shan ahead of the northward Pamir indentation. At 15.0 Ma, the appearance of North Pamir-sourced conglomerates followed at 11 Ma by Central Pamir-sourced volcanics coincides with a shift to E-W compression, clockwise vertical-axis rotations and the onset of growth strata associated with the activation of the local east vergent Qimugen thrust wedge. Together, this enables us to interpret that Pamir indentation into Tarim had started by 24.3 Ma, reached the study location by 15.0 Ma and had passed it by 11 Ma, providing kinematic constraints on proposed tectonic models involving intracontinental subduction and delamination.

1. Introduction

The uplift and formation of the Pamir orogeny (Figure 1) in response to the archetypal India-Asia continental collision have been linked to deep lithospheric processes of slab break off and roll back, continental subduction, and/or delamination (e.g., Chapman et al., 2017; Küfner et al., 2016; Sobel et al., 2013), as well as to surface processes of the Pamir plateau, and to Asian atmospheric circulation and related desertification (e.g., Caves et al., 2015; Thiede et al., 2013). However, the poor temporal resolution for this tectonic deformation generally precludes evaluation of regional geodynamic, geomorphic, and climatic models. To assess tectonic models, we date and analyze sedimentary successions that have recorded the Pamir tectonic evolution in the adjacent Tarim basin.

Tectonic models diverge in explaining the formation of the Pamir mountain range and its indentation into the Tajik and Tarim basins (*the Pamir salient*; Figure 1), in relation to the tomographically imaged southward dipping and 300-km long Alai slab (e.g., Negredo et al., 2007). There are currently two end-member tectonic models proposed to explain the Pamir evolution. The *subduction model* (Burtman & Molnar, 1993; Sobel et al., 2013) suggests that the Pamir terranes penetrated ~300 km northward into Tarim as a result of continental subduction-induced processes linked to roll back of the Alai slab constituted of Asian lithosphere. In that view, the Pamir is thought to have been, prior to its formation, a relatively straight east-west margin, aligned with the Kunlun mountain range and the northern margin of Tibet. In the alternative *delamination model* (Bird, 1979), the Pamir formed from northward underthrusting of the Indian plate, which forced the delamination and rollback of the Alai slab constituted either of Asian (Küfner

10.1029/2018TC005146

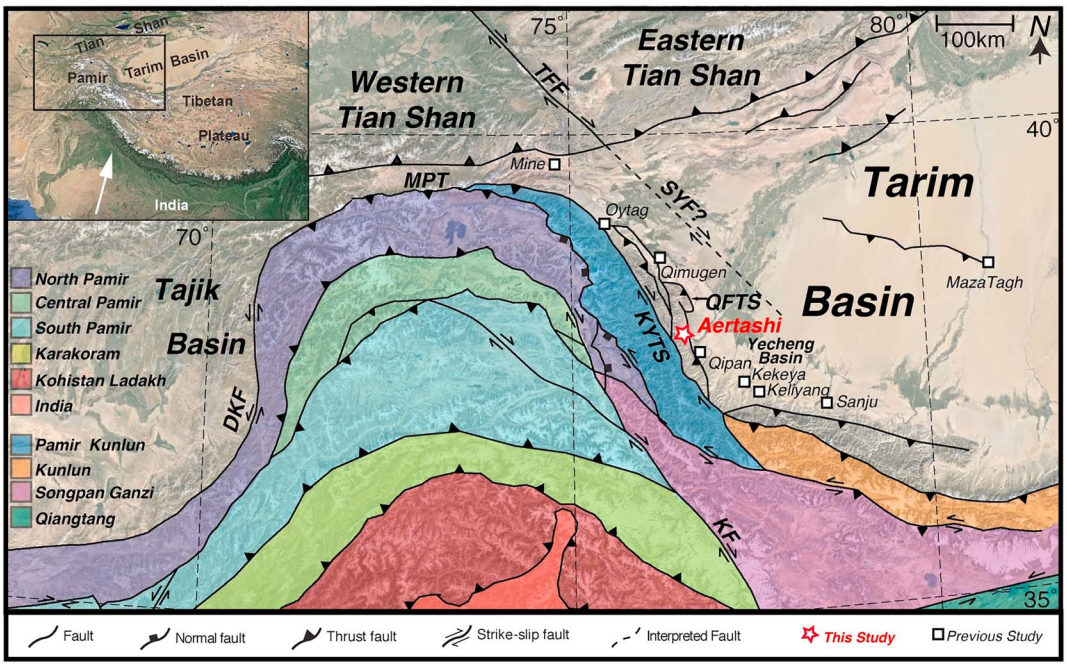

Figure 1. Geological setting and location (adapted from Sippl et al., 2013) showing major tectonic structures (HeF = Herat Fault, SS Shyok suture, DKF = Darvaz-Karakul Fault System, MPT = Main Pamir Thrust, TFF = Talas Ferghana fault, SYF = Sache-Yangdaman fault, KYTS = Kashgar-Yecheng Transfer System, KF = Karakorum fault, QFTS = Qimugen Fold Thrust System).

et al., 2016) or Pamir (Chapman et al., 2017) mantle lithosphere. In the delamination end-member, the indentation occurs in deeper levels of the lithospheric mantle such that northward crustal shortening is not required to account for the entire indentation; the indentation is more likely expressed by crustal exhumation and surface uplift (Chapman et al., 2017). However, assuming no or very limited shortening ultimately implies that the arcuate shape of the Pamir salient is an inherited older structure.

These end-member models make specific predictions regarding the timing and evolution of the Pamir salient that are recorded in adjacent basins. The subduction model requires, since circa 25–20 Ma, 300 km of underthrusting of the Tarim-Tajik basins beneath the Pamir crustal salient (Sobel et al., 2013). This indentation should be accommodated in the same period by the same amount of strike-slip motion and/or vertical axis rotations on the sides of the Pamir salient (Cowgill, 2010). The delamination models suggest thickening and uplift within the Pamir propagated from south to north in response to 300 km of indentation of the Indian mantle lithosphere since 10 Ma (Küfner et al., 2016) or since 22 Ma (Chapman et al., 2017). The latter model is based on evidence for limited crustal deformation (circa 30–60 km) in the Tajik basin at odds with previous larger estimates (e.g., Bourgeois et al., 1997; Burtman & Molnar, 1993; Thomas et al., 1996).

To investigate the tectonic evolution of the Pamir, we focus here on the southwestern Tarim basin, containing a nearly complete >10-km sedimentary record (Jia, 1997), which today is flanked by the Pamir to the east and the Kunlun to the south (Figure 1). In many outcrop and subsurface sections across the southwestern Tarim basin, the onset of coarse clastic deposition and the occurrence of growth strata along with changes in provenance of clastic detritus have been reported and related to the thrusting and uplift of the nearby Pamir and Kunlun ranges (e.g., Cao et al., 2015; Wang & Wang, 2016; Wei et al., 2013). What remains unclear is the age of this deformation, partly because the chronostratigraphy of these sections remains insufficiently constrained. As a result, observed facies or provenance changes cannot be unequivocally related to hinterland tectonic deformation and to source exhumation dated with thermochronology.

In order to better constrain this evolution, we studied the Cenozoic Aertashi sedimentary section that constitutes the most complete and best-dated sedimentary Cenozoic sequences from the western Tarim basin (e.g., Wei et al., 2018; Yin et al., 2002; Zheng et al., 2010, 2015a, 2015b). This work follows and complements previous dating and provenance results from this section (Blayney et al., 2016; Bosboom et al., 2011, 2014a)

by providing (1) a sedimentological analysis of depositional environments, (2) magnetostratigraphic dating, (3) anisotropy of magnetic susceptibility analysis for stress orientation, (4) vertical-axis rotation analysis, (5) backstripping analysis, and (6) additional provenance data in key intervals. These results are discussed in light of a regional chronostratigraphic overview to reconstruct the regional evolution of the western Tarim basin and its relation to the Pamir indentation.

2. Geological Background

2.1. The Pamir

Located directly north of the western syntaxis of the Himalaya, the Pamir forms a high-elevation salient, extending north from the northern boundary of the Tibetan plateau to the southern Tian Shan and flanked by the Tarim basin to its east and the Tajik basin to its west (Figure 1). The eastern limb of the arcuate Pamir is often referred to as the *Pamir Kunlun* as it is regarded as a continuation of the east-west trending Kunlun range that forms the northern boundary of the Tibetan plateau (Blayney et al., 2016; Burtman & Molnar, 1993).

The Pamir is structurally bounded to the north by the Main Pamir Thrust (MPT) and by the strike-slip systems along its margins that include the dextral Kashgar-Yecheng Transfer System (KYTS) along the eastern side and the sinistral Darvaz-Karakul Fault system to the west (Burtman & Molnar, 1993; Cowgill, 2010). The structural activity of the latter is still poorly constrained in age and slip magnitude, although structural reconstructions have suggested that several hundred kilometers of the propagation of the Pamir can be accounted by vertical-axis counterclockwise crustal rotations in the Tajik basin (Bourgeois et al., 1997; Thomas et al., 1996). However, recent structural analyses of the Tajik basin and western Pamir considerably reduced these estimates to several tens of kilometers (Chapman et al., 2017). On the eastern side, the dextral KYTS activation is suggested by thermochronology using detrital apatite fission track (AFT) analysis to indicate the onset of cooling on both side of the fault system around 25–20 Ma (Sobel & Dumitru, 1997). Slip estimates on the KYTS have been reviewed by Cowgill (2010) and proposed to be ~280 km based on the offset between current thrust traces of the MPT to the north and the Kunlun to the south. However, no definitive piercing point has yet been established. Cessation of slip since Pliocene times (~5–3 Ma) has been suggested by Sobel et al. (2011) based on thermochronologic age-based estimates for the incision of river gorges that are minimally offset by the KYTS. The lack of Pliocene offset has been related to the northward motion of Tarim relative to Eurasia, coherent with the Pamir until today as indicated by Global Positioning System data (Ischuk et al., 2013; Sobel et al., 2011; Zubovich et al., 2016).

The Pamir is constituted of accreted terranes (comprising the North, Central and South Pamir terranes respectively) that are proposed to be the western continuations of the Tibetan plateau terranes (the Songpan-Ganzi, Qiangtang, and Lhasa terranes) with varying interpretations for how these are correlated (e.g., Cowgill, 2010; Robinson, 2009, 2015). Large portions of the Pamir plateau exhibit exhumation of deep crustal levels through a set of core-complex domes (Rutte, Ratschbacher, Khan, et al., 2017, Rutte, Ratschbacher, Schneider, et al., 2017; Stübner, Ratschbacher, Rutte, et al., 2013, Stübner, Ratschbacher, Weise, et al., 2013). This suggests a very different deformation regime and history compared to the Tibetan plateau, which still exposes mostly upper crustal facies. In the Pamir, thickening of the continental crust up to 90 km is documented to have commenced prior to ~35 Ma based on the timing of prograde metamorphism (Stearns et al., 2015), and compression up to 22 Ma is documented in the Pamir terranes (Rutte, Ratschbacher, Khan, et al., 2017, Rutte, Ratschbacher, Schneider, et al., 2017; Stübner, Ratschbacher, Rutte, et al., 2013, Stübner, Ratschbacher, Weise, et al., 2013). This is followed from 22 to 12 Ma by the formation of bivergent N-S extensional core-complex domes interpreted as extensional collapse of the thickened crust (Carrapa et al., 2014; Rutte, Ratschbacher, Khan, et al., 2017; Rutte, Ratschbacher, Schneider, et al., 2017; Stübner, Ratschbacher, Weise, et al., 2013; Thiede et al., 2013). Since 12 Ma, N-S compression is indicated by inversion of the dome structures in the Pamir, and compression and exhumation in the western as well as the eastern Tien Shan (e.g., Charreau et al., 2009; Heermance et al., 2007; Käßner et al., 2016; Liu et al., 2017; Sobel et al., 2006). However, within the eastern Pamir Limb E-W dome extension occurred along the E-W Kongur Shan extensional system since 12 Ma (Robinson et al., 2007) and has been associated with volcanic eruptions of deeply sourced material such as the Dunkeldik volcanics (Kooijman et al., 2017).

2.2. The Western Tarim Basin

The western Tarim basin forms part of a relatively undeformed crustal block of Archean and Proterozoic metamorphic units overlain by Palaeozoic, Mesozoic, and Cenozoic marine to continental sedimentary rocks (e.g., Zheng et al., 2010). During the Cenozoic, the western Tarim basin has been subjected to overthrusting along its margin by the Tien Shan in the north, the Kunlun Shan in the south, and the Pamir in the west (e.g., Burtman & Molnar, 1993; Cowgill, 2010; Jia, 1997; Yin & Harrison, 2000). Thick sedimentary sequences provide a record of the tectonic activity along the margins of the basin. Cenozoic sedimentation in the western Tarim basin starts with deposition of the Palaeogene Kashi Group, composed of the Aertashi, Qimugen, Kalatar, Wulagen, and Bashibulake formations. These formations are predominantly composed of marine facies, providing reliable markers for regional lithostratigraphic correlations with age control from biostratigraphy (Bosboom et al., 2011, 2014b; Lan & Wei, 1995; Mao & Norris, 1988; Tang et al., 1989). After the Eocene Tarim sea retreat, the western Tarim basin was filled by a series of thick terrestrial red clastic units known as the Wuqia Group (Keziluoyi, Anjuan, and Pakabulake formations) overlain by the Atushi formation (e.g., Yin et al., 2002). These mainly consist of sandstone interbedded with clay and siltstones dominated by continental fluvial deposits ranging from meandering stream facies to braided river deposits and lacustrine and floodplain deposits (e.g., Yin et al., 2002; Zheng et al., 2015a; Zhou, 2000). In principle, these red bed formations can be dated by magnetostratigraphy; however, their age and correlation across the basin remain controversial (e.g., Zheng et al., 2015a, 2015b). The overlying Xiyu formation is dominated by thick successions of gray to brown conglomerates typical of alluvial fan environments (Teng et al., 1996; Zheng et al., 2006, 2015a). The deposition of the Xiyu formation is highly diachronous. Its base has yielded various ages at different locations, from 16 Ma to <1 Ma (Charreau et al., 2006; Heermance et al., 2007; Sun et al., 2004, 2007; Teng et al., 1996; Yang et al., 2015; Zheng et al., 2000). Rare volcanic horizons have been recently dated at around 11 Ma at two locations, providing additional age control (Zheng et al., 2015a, 2015b; Sun et al., 2015). Despite a large amount of surface and subsurface data, the tectonic evolution of the western Tarim basin remains poorly constrained, in part due to the difficulties associated with basin-scale correlation of the various sedimentary formations that remain to be accurately dated.

2.3. The Yecheng Sub-Basin and the Aertashi Section

The study area is located near the village of Aertashi in the western Yecheng sub-basin along the margin of the Pamir Kunlun (Figure 1). The Yecheng sub-basin has been interpreted by Wei et al. (2013) as a transtensional *pull apart* basin, formed in the Miocene as a result of the synchronous activity of the KYTS and the right-lateral Sache-Yangdaman fault (SYF), which is now in the subsurface cutting the basement and some of the overlying strata. The existence of the SYF and its transtentional nature is interpreted based on flower structures observed in seismic data. The structures are covered by unaffected strata attributed to the Miocene, and their lateral extent is not yet constrained (Wei et al., 2013). The Aertashi section is located within a west-directed thrust sheet identified by seismic data and referred to as the Qimugen Fold Thrust System (QFTS) with associated growth strata of unknown age (Figure 1, Wang & Wang, 2016; Wei et al., 2013). The age of the strata and thrusting will be estimated using the dating of the stratigraphy of the Aertashi section presented in this study complemented by a regional review of chronostratigraphic studies.

Within the Aertashi section, Paleogene-Neogene eastward dipping sedimentary rocks are well exposed (from 76.5462°E; 37.9714°N to 76.6055°E; 37.9898°N) along river drainages and the roadside from the village of Aertashi toward Poskam. They provide a continuous record of the transition from marine facies of the Kashi Group to a continental fluvial system in the Wuqia Group. Within the sampled 4,000-m thick section, there is no evidence of major faulting or folding that could affect the sedimentary record.

Previous work on sedimentology at this section identified the underlying Kashi group as a series of marine successions including the Aertashi, Qimugen, Kalatar, and Wulagen formations that record marine transgression-regressions cycles of the Tarim Sea (e.g., Bosboom et al., 2011, 2014b). Overlying these rocks are a series of terrestrial red sandstones, siltstones, and mudstones interpreted to be fluvial, lake, and delta facies of the nonmarine Bashibulake formation and the overlying Wuqia Group. An abrupt change in lithofacies is recorded in the overlying conglomeratic Xiyu formation (Zheng et al., 2010, 2015a).

Previous investigations on the Aertashi section also includes Yin et al. (2002), which combined sedimentology and magnetostratigraphy of the red beds of the Wuqia Group below the Xiyu formation. However, given

the low sampling resolution of 22.5 m, this study was insufficient to make an accurate correlation with the geomagnetic polarity timescale (GPTS). It thus yielded a number of possible correlations from 31–24 Ma or from 20–15 Ma for the section under study, with a high level of ambiguity. Bosboom et al. (2011, 2014a, 2014b) conducted a combined biostratigraphic and magnetostratigraphic analysis of the Kashi Group and the lower part of the Wuqia Group at the Aertashi section. They recognized the last marine deposits at Aertashi as belonging to the Wulagen formation with a Late Eocene age constrained by bivalves, calcareous nanofossils, and dinoflagellate cysts. Based on magnetostratigraphy, they further indicated that the start of the continental section lies at the base of C18r (circa 41 Ma) and dated through to C9.n (circa 27 Ma). More recently, the upper part of this section has been dated by Zheng et al. (2015a) using magnetostratigraphy, combined with the basal constraints of Bosboom et al. (2014a), and an upper depositional age of 11-Ma constraint provided by Ar-Ar age control from a volcanic ash layer (Wei et al., 2018). In a previous paper, Blayney et al. (2016) provided provenance analysis of the Aertashi section based on detrital zircon U-Pb ages coupled with zircon fission track, bulk rock Sm-Nd, and petrography data. They interpreted the results to show (1) from 41 to circa 25 Ma, provenance mainly from the Kunlun to the south and from further south into the Central Pamir and Songpan-Ganzi and Qiangtang terranes; (2) from circa 25 Ma, a subtle provenance change interpreted as Kunlun uplift shutting off the southerly sources; and (3) at circa 14 Ma, the arrival of detritus from the northern Pamir terrane. These ages and provenance results will be revised in the following analyses.

3. Results and Analysis

3.1. Sedimentological Analyses

We present here the complete sedimentologic analysis of the Aertashi section from the onset of continental deposits after the 41-Ma sea retreat to the onset of conglomeratic deposits of the Xiyu formation.

We use the Miall (1985) approach for facies analysis and depositional environment interpretations with full facies descriptions and associations provided in Tables S1a and S1b in the supporting information and facies identification labeled in Figures 2 and 3. The stacking pattern of the successive depositional environments is interpreted in terms of changes in base level and accommodation space. The lithological descriptions were performed at a 1/100 scale throughout the section while sampling for magnetostratigraphy. Following up from the basal continental unit already described in Bosboom et al. (2011, 2014a, 2014b), we defined six sedimentary units (A–F) based on major changes in facies and depositional environments (Figure 2). For each unit, characteristic intervals were logged in more detail at a 1/40 scale; observations include lithology, grain size, sedimentary and biogenic structures, and palaeocurrent measurements (Figures 2 and 3, and Tables S1a and S1b). Unit ages are already indicated for convenience but are based on magnetostratigraphic results presented later. The complete log is presented in Figure 5.

3.1.1. Basal Continental Unit (~41–35.6 Ma)

The onset of extended continental deposition in Aertashi commenced at the fourth marine regression at ~ 41 Ma (Bosboom et al., 2014a), with the last marine beds defining the 0-m level of the section. The lower part of the stratigraphic section, from 0 to 760 m, is characterized by red siltstones to medium-grained sandstones with cross stratification and incised channel fills interbedded with gypsiferous mudstones. These facies are interpreted to represent dominantly alluvial floodplain deposits with occasional (brackish) lacustrine intervals (Bosboom et al., 2014a). This part has been dated from ~ 41 to ~ 36 Ma in age, with a marked hiatus at ~760 m, dated from circa 36 to 33 Ma that has been interpreted to result from a base level drop at the Eocene-Oligocene transition (Bosboom et al., 2014a).

3.1.2. Unit A: Aeolian Dune, Interdune, and Arid Floodplain Deposits (33.0–32.2 Ma)

The lower part is ~20-m thick and composed of massive, well-sorted, pinkish, medium-grained sandstones. The sedimentary structures show alternations of meter-scale trough cross bedding and centimeter-scale rippled and low angle planar laminated beds. The upper part of the large cross-beds exhibits inverse grading typical of avalanche deposits where their lower part wedge out in millimeter-scale wind-ripple laminas (Figures 2a and 2b).

The upper part is 25-m thick and composed of 3- to 5-m-thick sequences of pinkish to reddish brown medium-grained locally coarse sandstones, siltstones, and minor gypsiferous mudstones alternations (Figure 2b). The mudstone content increases up-section. At the base, the sequences are composed of thick

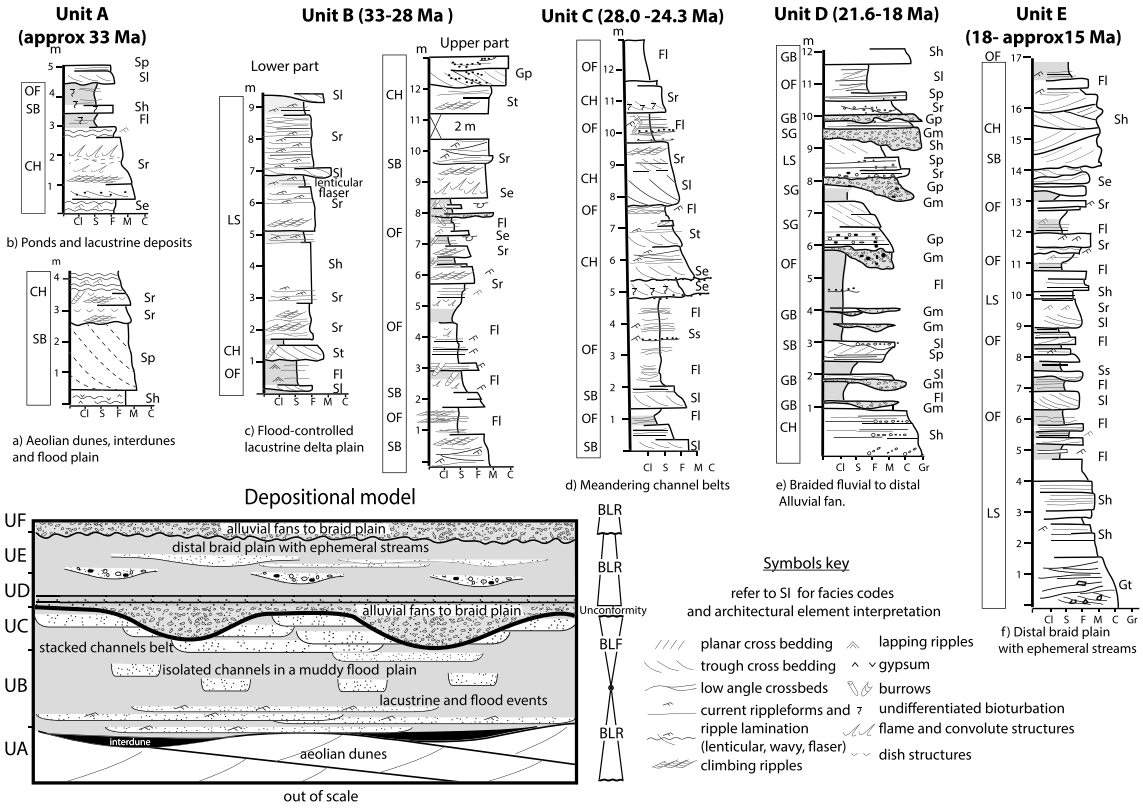

Figure 2. Top part shows detailed sedimentary logs taken from representative intervals of the studied units of the Aertashi section. For each log, the left-hand column includes architectural elements: laminated sand sheets (LS), sandy bedforms (SB), overbank fines (OF), channelized sandstones (CH), gravel bars (GB), sedimentary gravity flow (SG). Labels on the right of the logs refer to facies associations following Miall (1985; see Tables S1a and S1b). Lower panel shows the depositional model for (UA-F) of the Aertashi section. BLF = base-level fall, BLR = base-level rise.

sandstone beds with large cross beds, as described above, alternating with decimeter-scale, fining upward sandstone and siltstone beds with climbing ripples, dish structures, and bioturbation structures at the top (Table S1a and S1b and Figure 2b). Up-section, the large cross-stratified beds disappear while rippled beds with convolute and dish structures interbedded with bioturbated red siltstone and mudstone become predominant. The main facies interpretations for unit A consist of channelized sandstones (CH), overbank fines (OF), and sandy bedforms (SB).

The large cross-beds in the lower part of unit A are interpreted to be aeolian dune deposits. These are interbedded up-section with waterlain rippled deposits with gypsiferous nodules deposited rapidly in shallow ponds or interdune environments. Up-section, the aeolian dune deposits disappear, giving rise to larger ponds or lakes in a muddy floodplain environment with occasional crevasse splays. The presence of abundant gypsum at the base of the unit points to an arid or semiarid environment.

3.1.3. Unit B: Flood-Controlled Lacustrine Sandy Delta Plain Deposits (32.2–27.4 Ma)

The contact between units A and B is gradual. Unit B is ~670-m thick (820 to ~1,490 m) and made up of fine- to medium-grained sandstones alternating with minor red silts and clays (Figure 2a).

The lower part is composed of 10-m-scale fine- to medium-grained, reddish brown, clayey sandstones, which alternate with decimeter-scale red muddy siltstones. The sandstones show fining upward centimeter to 50-cm-thick beds. In the most complete sequences, the beds comprise high-energy planar and climbing ripple (flaser to lenticular) laminations capped by low-energy planar laminations or a centimeter-scale clay drape (Figure 2c and Tables S1a and S1b). In places, these rippled sandstones are cut by fining upward, centimeter-thick and 10-m-wide, flat channels of medium to coarse sandstones with low angle lamination, overlain by bioturbated red silty mud with flaser and lenticular bedding and lapping ripples (Figure 2c). The upper part is more heterolithic with a few meter-thick fine-grained sections alternating with well-sorted sandstone bars and gravelly sandstone channels. The fine-grained sections show fining upward sequences of rippled

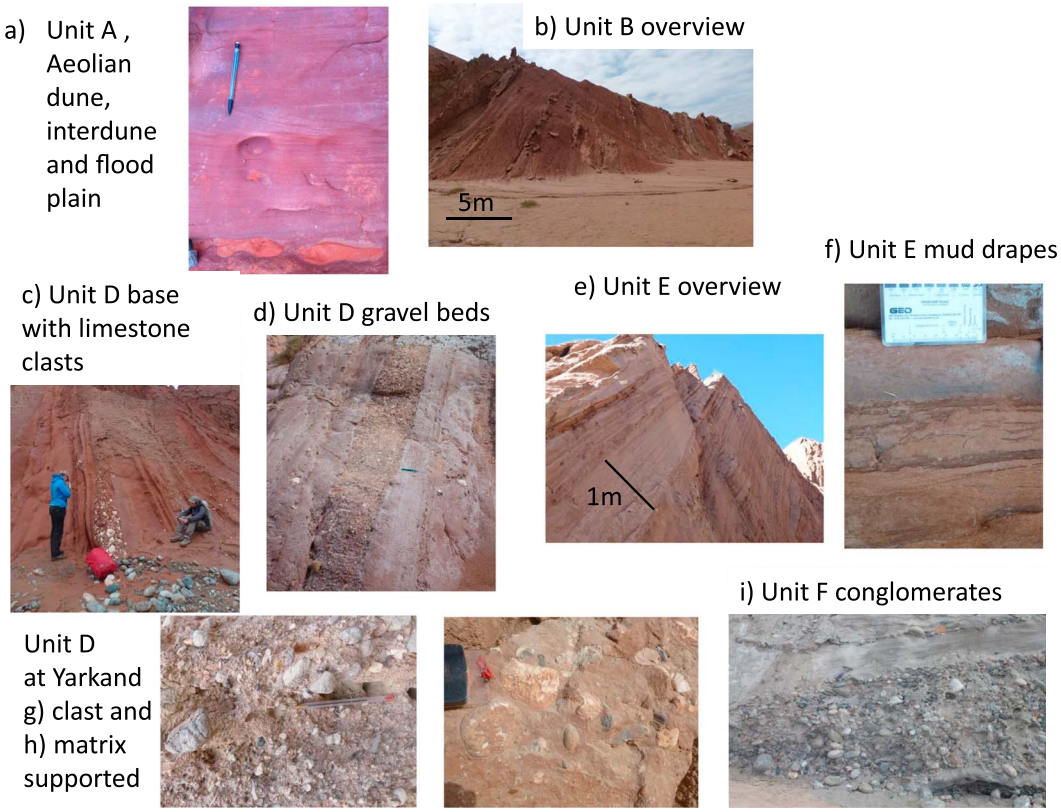

Figure 3. Images of the main sedimentological units in the study section (a) Close-up of unit A aeolian dune, interdune, and floodplain facies, (b) an overview of unit B showing large-scale cycles of medium-coarse sandstone, interbedded with siltstones and clays, (c) unit D base with typical conglomerate beds containing abundant large limestone clasts interbedded with medium to fine sandstones and siltstones, (d) overview of planar gravel beds within unit D containing abundant limestone and sandstone clasts. (e) overview of unit E, (f) close-up image of unit E showing cross bedding overlain by mud drapes and sandstone beds, (g) image of the unit D conglomerates from Yarkand section showing clast-supported structure and (h) matrix-supported structure, (i) overview of unit F conglomerates from Aertashi interlayered with grey sandstones, geological hammer used for scale.

sandstone and bioturbated siltstones with intervening pebbly gutter casts. The sandstone sections show large rippled cross bedding with dewatering structures where gravelly channels exhibit trough bedding. Unit B consists of mainly SB, OF, and CH.

The rippled fining upward sequences in unit B are interpreted as flood deposits (splays) in a highly efficient laminar flow fluvial system of a lacustrine delta plain. At the base of unit B, during the dry season, small, shallow crevasse splay channels overlain by muddy ponds incise the delta plain. At the top of the unit, the fine red mud brought by the successive flood events in the floodplain is more abundant. The muds reduce channel wandering, leading to an increase in channel size in order to drain the floodplain and build large rippled, cross-bedded bars along their main conduits. In places, the top of the channel fills and crevasse splays is filled by pebbly to gravelly material deposited during flash floods.

3.1.4. Unit C: Stacked Fluvial Meandering Channel Belts (27.4–24.3 Ma)

The transition from unit B to unit C is gradual. Unit C is ~560-m thick (~1,490–2,050 m) and made up of decimeter-thick alternations of red siltstones/fine sandstones and medium- to coarse-grained sandstones (Figure 2d and Tables S1a and S1b). The fine material shows centimeter-scale rippled beds with millimeter-scale mud pebbles interbedded with microlaminated silts with clay drapes. The fines are cut in places by decimeter-scale fining-up sandstone crevasse channels with bioturbated tops. The sandstones show a channelized erosive base overlain by fining and thinning upward stacks of beds with trough cross laminations and ripple laminations at the top. Occasionally, at the top of the unit, the basal erosional surface is filled with pebbles and cobbles of carbonate, sandstones and occasional basement rocks. Unit C is mainly composed of sequences of SB, CH, and OF.

We interpret the cross-bedded sandstones to be large stacks of channels filled by sinuous crested bedforms produced by high-energy flows. These channel belts are bounded by thin layers of fine-grained material settled in a floodplain environment, which is frequently flooded as shown by the varve-like silt-clay couplets, the scarcity of crevasse splay deposits, and pedogenesis horizons.

3.1.5. Unit D: Proximal Alluvial Fan to Braided Plain Deposits (21.6–18.1 Ma)

Unit D is 740-m thick (2,050–2,790 m) at Aertashi; the contact between units C and D is marked by an erosional unconformity. Unit D is a gravelly unit with interbedded medium red sandstones, siltstones, and clays (Figure 2e and Tables S1a and S1b). The basal beds contain large isolated limestones clasts of up to 0.5 m in diameter supported by a cross-bedded sandy matrix. Unit D is typically made up of stacked, meter-scale, fining upward sequences with an overall fining upward trend and increasing upward proportion of red, fine-grained material. Clasts are predominantly composed of limestones and sandstones with rare igneous and metamorphic clasts, that is, surficial sedimentary cover rather than of the underlying basement.

A typical complete sequence is composed of a massive, matrix (sand) supported, coarse gravel beds, overlain by pebbly (and occasionally cobble) sized clasts (Figure 3c) with planar horizontal lamination (Figure 3d) and trough cross-bedded sands. The sequence is capped by planar horizontal lamination in sandy silt and massive red silts with occasional floating pebbles. The latter show thinning and fining upward successions of planar and trough cross stratified, centimeter-scale sand beds with normal and reverse grading. Unit D is composed of predominantly gravel bars and bedforms with sediment gravity flows and occasional laminated sand sheets, OF, and CH (Tables S1a and S1b and Figure 2e).

Unit D is interpreted to represent the toe of a distant alluvial fan with ephemeral braided streams feeding a semiarid floodplain. The proximity of the fan break in slope is indicated by the presence of oversized blocks, the abundance of debris flows, and the floating pebbles in the red mudstones. The conglomerates of unit D extend over a horizontal (along strike) distance of approximately 40 km (Figures 3g, 3h, and 4) as mapped in the field and using Google Earth. They disappear toward the north but thicken toward the south as observed at the Yarkand section. There, the measured thickness of the unit is estimated to be 1,050-m thick between the upper (N37°48′02.1″ E076 37′33.9″) and lower (N37°47′52.1E076 36′29.4) contacts with an average bedding attitude of 042°/62° (dip direction and dip). This is clearly thicker than the measured 740 m at the Aertashi section, showing that these conglomerates thicken substantially to the south. In addition, the conglomerates at Yarkand exhibit both clast-supported and matrix-supported structures (Figures 3g and 3h); clasts are generally larger than at Aertashi further suggesting a more proximal position with respect to the source.

3.1.6. Unit E: Distal Braid Plain With Ephemeral Streams (18.1–15.0 Ma)

There is a gradual coarse to fine transition between unit D and unit E, observed by a reduction in gravel beds and an increase in sandstone and mudstone beds. Unit E is 1,260 m-thick (2,790–4,050 m), composed of a coarser lower sub-unit Ea and a finer sub-unit Eb. These are arbitrarily separated at the highest observed gravelly conglomerate bed in unit E at 3,020 m. Typical successions of unit E are composed of decimeter-thick packages of gravelly sands, sands, silts, and red mudstones. These successions first thin and fine upward and then thicken and coarsen upward (Tables S1a and S1b and Figure 2f). The bases of these individual facies successions are marked by erosion surfaces (Se), in places scoured (Ss), that display the morphology of 1-m deep and 10-m wide, smooth shallow channels. The channels are filled by trough cross-bedded sands with some floating pebbles organized in low-angle lateral accretion bedding. The overlying sandstone beds that fill up the channels are predominantly low angle to horizontally laminated (Sh) with occasional trough cross-laminations (St) while red silts and clays drape their top. The fine-grained part that makes up the majority of the facies succession is sets of 1- to 2-m fining up sequences with thick medium to fine sandstones with low-angle cross-bedded bases that grade into ripple laminations (Sr) with fine-laminated clays and silts (Fl) at the top of the sequence (Figure 2f). Unit E has four facies associations, predominantly laminated sand sheets and OF with occasional SB and CH.

Unit E is interpreted to be distal alluvial with abundant crevasse and flood deposits produced by highly efficient shallow, meandering channels. The presence of floating pebbles and coarse-grained sand, the low-angle lamination and lateral-accretion bedding points to a predominance of ephemeral streams fed by laminar flash floods at the distal part of the coarse alluvial fan or braid plain, and the gradual fining upward throughout unit E reflects increasingly distal alluvial fan depositions.

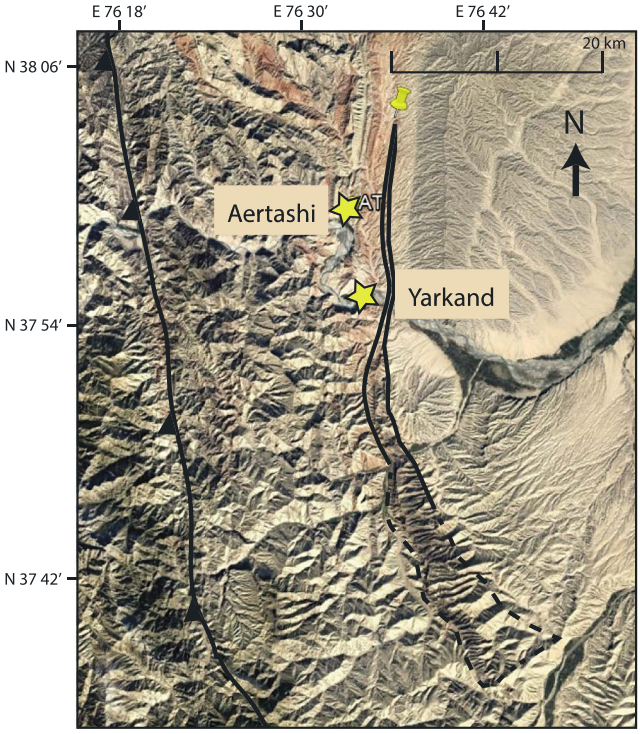

Figure 4. Extent and geometry of the conglomeratic unit D along the western Kunlun showing thickening and coarsening to the south as observed between the Aertashi and Yarkand sections. Image is from Google Earth.

3.1.7. Unit F: Proximal Alluvial Fan (15–11 Ma)

Unit F (above 4,050 m) is dominated by large clast-supported cobble conglomerates (Figure 3i). A gradual change precedes the onset of unit F within the top 50 m of unit E, where gray gravelly beds are occasionally interlayered within the finer red beds. The composition of these gravels is similar to that observed in the clasts of the overlying conglomerates of unit F. Clasts of unit F are well rounded and up to 30 cm in diameter with clear imbrication structures. These conglomerates contain basement rocks and volcanic pebbles; they are clast supported and clasts are generally much larger and more rounded than those observed in the lower conglomerates of unit D. The unit is reported to extend upward another 2.4 km up to the 11-Ma volcanic units (Wei et al., 2018).

3.1.8. Sedimentology Summary and Interpretations

Three major changes marked by depositional shifts are found in the studied section: one at the base of unit A, one at the base of unit D, and one at the base of unit F. These surfaces correspond to periods of relief rejuvenation and/or regional deformation as summarized below. These surfaces bound depositional megasequences that provide an insight into the overall development of the landscape through time. The first megasequence boundary is marked by a disconformity at circa 740 m. Its age ranges from 35.6 to 33.0 Ma (Bosboom et al., 2014a, Figure 5). It has been interpreted to result from a major base level drop associated with the circa 100-m eustatic drop at the 34-Ma Eocene-Oligocene transition (Bosboom et al., 2014a). Above this, units A, B, and C show the evolution from a very arid environment with large aeolian dune deposits (unit A) passing upward into wet interdunes and ponds to a lacustrine delta plain (unit B base) with highly efficient flows that transported a large volume of sandy material. The lacustrine delta plain evolves progressively up-section into a dryer, distal, muddy floodplain with isolated meandering channels (unit B top). These channels progressively amalgamate into channel belts in unit C, suggesting the accommodation space decreases sharply (Shanley & McCabe, 1993) before the onset of the unit D, which defines the next megasequence boundary. Proximal alluvial fan to braid plain deposits of unit D sharply overly distal fluvial, meandering channel belts of unit C. The base of unit D corresponds to a large depositional hiatus as shown by the magnetostratigraphic result presented below. This and the sharp facies change indicate a drastic basinward shift of the facies belts and depositional environments, interpreted as a consequence of relief formation. The sediments above the unconformity show an increasing accommodation space (see next section on magnetostratigraphic dating) with an evolution from proximal to more distal environments. Gravelly debris flow-dominated alluvial fan deposits in unit D shift up-section in unit E to fine-grained, muddy floodplain deposits, with sands fed by ephemeral streams and flash floods during rainy periods of a more distal alluvial fan environment. The sharp increase in grain size to cobble conglomerates at the base of unit F signals another sharp basinward shift of the facies belts with a large set of proximal alluvial fan deposits forming part of a distal braid plain.

3.2. Paleomagnetic Analysis and Results

Our study continues up-section from the point where the work of Bosboom et al. (2014a, 2014b, 2014c) terminates (at the 1,534-m level dated circa 27 Ma; 37°58.284′N, 076°34.785E). We therefore provide a complete and revised paleomagnetic analysis from the final sea retreat recorded by Bosboom et al. (2014b) all the way through to the onset of alluvial fan facies of unit F.

3.2.1. Sampling and Analyses

Paleomagnetic sampling at the Aertashi section was performed using a battery-operated electric drill with an air-cooled diamond bit, yielding standard core samples of 2.5 cm in diameter. Samples were orientated using a Pomeroy orienting tool with a Brunton magnetic compass and a clinometer. The sampling strategy involved digging trenches to preferentially sample the finest grain size in order to prioritize the single-domain magnetic particles that are more stable at longer timescales (Butler, 1992) and because the smallest grains are the most likely to align with the field during deposition. Four hundred ninety-six samples were

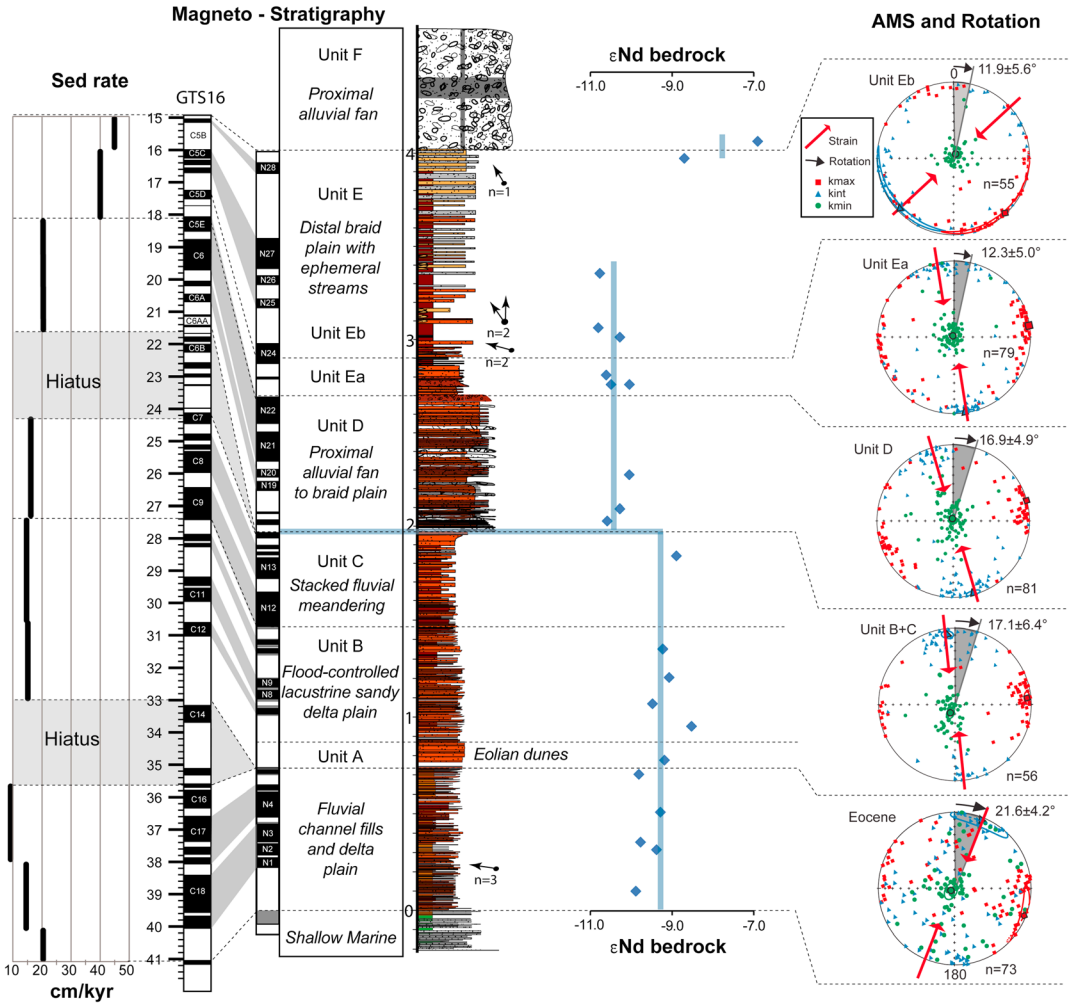

Figure 5. Log of the Aertashi section with sediment accumulation rates (Sed rate) plotted against interpreted polarity zones with the preferred magnetostratigraphic correlation to the Geomagnetic Polarity Time Scale of Ogg et al. (2016); for detailed results, see Figure 8. Facies unit classification and interpreted depositional environments as described in this study and supporting information part 1. εNd data combined from Blayney et al. (2016) and this study (Table S6). AMS principal directions plotted on stereographic projections with interpreted principal strain directions indicated with red arrows (Figure S6 and Table S5). AMS data are corrected for the vertical axis rotations. These rotations are derived from ChRM direction means with respect to the Apparent Polar Wander Path of Eurasia (supporting information part 2, Table S3) and indicated by black arrows for each interval. AMS = anisotropy of magnetic susceptibility; ChRM = Characteristic Remanent Magnetization.

collected over 2,500 m of section at a resolution of 0.4–5 m. Occasional sampling gaps are minimal (<40 m) due to the exceptionally continuous outcrop; deeper trenches were dug in less well-exposed parts. Following fieldwork, samples were cut into cores of 2.2 cm in length.

Analysis was performed in the magnetically shielded room at the archeo-palaeomagnetic laboratory at the University of Rennes 1. A first set of pilot samples were processed using alternating field and thermal demagnetizations in a shielded oven in order to determine the best processing strategy and identify potential magnetization carriers. Thermal demagnetization yielded better results; therefore, this technique was then applied to subsequently processed samples using 10–18 temperature steps between room temperature and 690 °C. The remanent magnetization was measured using a 2G cryogenic magnetometer. To monitor mineral transformation upon laboratory heating, bulk magnetic susceptibility was measured at room temperature for each sample between each temperature step using a Bartington MS2 magnetic susceptibility meter.

3.2.2. Characteristic Remanent Magnetization

In total 451 samples were demagnetized. The remaining 45 samples were not processed because they were considered not necessary to better define the paleomagnetic polarity zones and reversal pattern. Demagnetizations for each sample are provided in the supporting information (Database S1). Between room temperature to 250 °C progressive removal of a secondary magnetic overprint was observed. Subsequent demagnetization trajectories showed, in most samples, a linear decay toward the origin above ~350 °C down to 670–680 °C, suggesting a minor content of magnetite and a major content of hematite that demagnetized between 600–650 and 660–690 °C. This component was used to determine the Characteristic Remanent Magnetization (ChRM) directions. In a few samples from coarser red sands of the base of unit E, demagnetization in the same temperature range was often more erratic, yielding less precise or uninterpretable directions.

The ChRM directions were calculated for orthogonal plots using principal component analysis (Kirschvink, 1980). Line fits were determined using a minimum of four temperature steps (Figure S3A). In very rare cases (23), line fits were forced through the origin where directions were clustered in a distinct normal or reverse direction but did not decay to the origin. Four-hundred fifty line fits were obtained and categorized into quality 1, 2, or 3, depending on the reliability of the results defined as follows (Table S4). *Quality 1* (*Q1*) - ChRM direction (declination and inclination) was precisely determined and the polarity (normal or reversed) unambiguously identified. *Quality 2* (*Q2*) - ChRM direction were less precise but the polarity was well established and could be unambiguously determined. *Quality 3* (*Q3*) - the polarity could not be determined from the ChRM directions. These 44 Q3 ChRM directions and 9 ChRM directions with maximum angular deviation over 30° were rejected from further analysis. The remaining ChRM directions have an average maximum angular deviation of 12.7°. On these directions, the iterative cutoff criteria of Vandamme (1994) were applied separately on normal and reversed polarity directions, resulting in a further removal of 57 transitional and outlying directions (Figure S3b). The Virtual Geomagnetic Pole latitudes were calculated from the obtained ChRM directions. The remaining 350 directions separate into two antipodal clusters from which the mean normal and reversed ChRM directions were calculated (Fisher, 1953; Figure S3b). A fold test was not applicable because of insufficient bedding attitude variations through these mostly homoclinal successions. However, A reversal test was performed (Tauxe, 1998) to determine the primary origin of the magnetization (Figure S3c). This yielded a positive result suggesting a primary origin of the ChRM directions. These directions were thus used for defining polarity zones to be correlated with the GPTS (Figure S4).

3.2.3. Magnetostratigraphic Correlation and Accumulation Rates

Following interpretation of the primary origin of the magnetization, polarity zones identified in Aertashi could be correlated with the GPTS (Ogg et al., 2016); (Figures 5 and S4). Polarity zones were defined by at least two consecutive Virtual Geomagnetic Pole latitudes of identical polarity, leaving any isolated directions within a polarity interval of opposing polarity rejected. Polarity zones were numbered from N12 to N28 following on from the numbering scheme defined by Bosboom et al. (2014a) for the lower part of the Aertashi section, from which this work is a continuation.

A basal constraint is provided for the Aertashi section by Bosboom et al. (2014a), who defined a correlation between N12 to C9n. Following on from the basal correlation, the next normal zone of N13 can be correlated directly with C8n. However, polarity zones from N14 to N20 cannot be unambiguously correlated. We therefore start from the upper part of the section where the longest normal polarity zones are found. There, given that the record must be above C8n, a unique correlation of the observed polarity pattern can be readily identified as follows. The long reversed C5Br and C5Dr correspond, respectively, to R28 and R25 separated by the peculiar suite of three normal chrons of C5C corresponding to N27, N26, and N25, respectively. It follows upward that N28 corresponds to C5B.2n and downward that R24 corresponds to C5Dn, N23 to C5Dn.1n, and N22 and N21 to C5En and C6n (Figures 5 and S4). These constraints provide clear age determination for the bottom and top of the sampled section, respectively, at 27.0 and 15.0 Ma. This fits well with the independent 14.05 ± 0.85-Ma youngest U/Pb age from detrital zircons from the conglomerates directly overlying the sampled section (Blayney et al., 2016). However, the correlation remains ambiguous between N21 and N13, where too few polarity zones must be correlated to the period between C7 and C6AAn, characterized by a large number of short chrons. This indicates that there must be one or more sediment accumulation hiatuses present, of which multiple correlations may be proposed. A satisfactory correlation in this interval has been identified by continuing up from the basal section using the accumulation rate defined by the

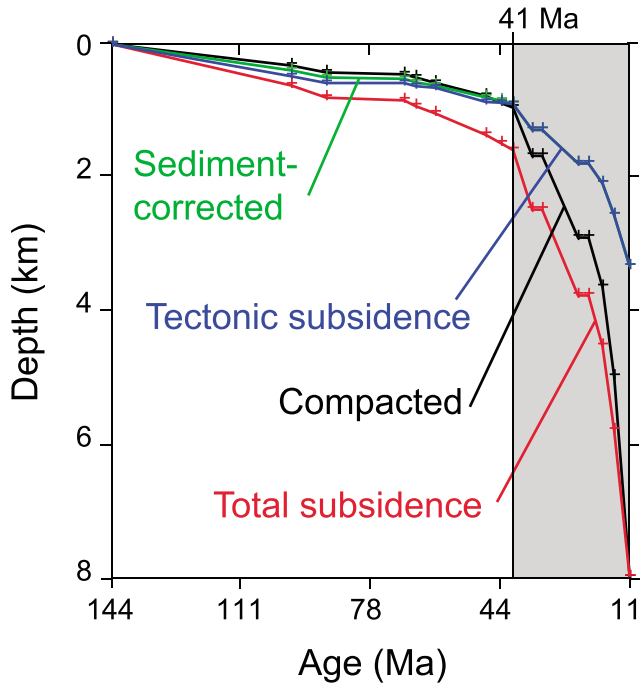

Figure 6. Backstripping model indicating tectonic subsidence for the Aertashi section using revised age control and formation thickness data from Sobel (1999), Bosboom et al. (2014b), and this study.

lowermost correlations, thus linking N15 to C7An and N16 to C7n. The same procedure was applied to the upper section by following the accumulation rate down the section, correlating N19 with C6An and N17 and N18 with the short normal chrons of C6AAn, which points to a single hiatus between C7 and C6AA (24.3 to 21.6 Ma) at ~1,935 m. This corresponds precisely to the major change in depositional environments between the fluvio-lacustrine facies of unit C below, to the conglomeratic braided facies of unit D above. Alternative viable correlations in this interval may be proposed but they are found less likely because they would involve multiple large variations in accumulation rates and/or depositional hiatuses that do not correspond to the observed changes in depositional environments.

From these age constraints, sediment accumulation rates can be determined using thicknesses between identified polarity zones of known age throughout the section (Figures 5 and S4). Accumulation rates for the basal part of the section from 41.0 to 24.3 Ma are fairly constant within 10–20 cm/kyr. However, following the hiatus recorded at the units C and D transition, accumulation rates increase from ~19 between 21.6 and 18.2 Ma to 41 cm/kyr between 18.2 and 16.0 Ma. Rates continue to increase toward the top of the section with a rate of 45 cm/kyr from 16.0 to 15.0 Ma before the onset of the proximal alluvial fan conglomerate deposition of unit F. The transition to unit F occurs within a few tens of meters stratigraphically (Figure 5) but is gradual with increased occurrences of gray gravelly beds within continuing red clastic beds suggesting no large hiatus. For the overlying Xiyu conglomerates, accumulation rates of 60 cm/kyr can be further estimated based on the 11-Ma deposition age provided by volcanic U/Pb zircons (Wei et al., 2018; Zheng et al., 2015a) stratigraphically positioned circa 2.4 km above the base of the conglomerates. This suggests sustained or increasing accumulation rates associated with the conglomerate deposits despite potential differential compaction effects.

3.3. Backstripping Analysis

We conducted modeling of the tectonic subsidence of the Aertashi section using the published data from Sobel (1999) with updated stratigraphy and age control from Bosboom et al. (2011, 2014a, 2014b) and this paper. Backstripping was performed with the Macintosh program, Backstrip (Cardozo, 2012), which is based on the methods of Van Hinte (1978) and Steckler and Watts (1978). We assigned a lithology-dependent density to every layer to create a density distribution within our sediments (Table S6). Factors for different lithologies were chosen in order to approximate porosity-depth relationships and correct for compaction effects. The two hiatuses recorded at 33.0–35.6 Ma (Bosboom et al., 2014a) and at 24.3 to 21.6 Ma (this study) were included in our model.

Our results identify the prominent onset of tectonic subsidence (subsidence that is not caused by the weight of sediments) at the base of the continental sediments at ~41 Ma (Figure 6). Above the 41-Ma regression, accumulation rates increase incrementally throughout the remainder of the section.

3.4. Tectonic Rotation

For our rotational analysis we followed the same methodologies reported in Bosboom et al. (2014c) using our magnetostratigraphic data sets that passed the reversals test (Figure S3 and Table S4) and thus provide average normal and reversed directions unbiased by secondary overprints. Antipodal reversed directions were rotated into normal and combined with normal directions to obtain, for the sampled section between 27.0 and 15.0 Ma, an overall average direction with calculation according to Fisher (1953); (before tilt correction: declination 334.7°, inclination 36.0°, and 95% confidence a_{95} 3.1°; after tilt-correction: declination 20.4°, inclination 33.1°, and 95% confidence a_{95} 3.1°; see Table S3). This averaged direction was compared to the expected directions for the Eurasian continent derived from the Eurasian Apparent Polar Wander Path at 20 Ma from Torsvik et al. (2012) to derive a 13.7° ± 3.9° clockwise vertical-axis rotation following

the methods of Demarest (1983). We compared our results with those of Bosboom et al. (2014c) and identified a systematic trend of decreasing clockwise rotation continuing throughout the section from 20.3° ± 4.4° between 41.0 and 35.6 Ma decreasing to 18.3° ± 6.4° between 33.0 and 27.0 Ma and our observed 13.7° ± 3.9° from 27.0 to 15.0 Ma (Figure 5 and Table S3). This indicates that most of the clockwise rotation (14° ± 4°) occurred after 15.0 Ma and only a small part of the rotation (7 ± 6°) occurred between 41.0 and 27.0 Ma. This is at variance with previous work that proposed that most tectonic rotation ceased by the end of the Oligocene on the eastern side of the Pamir (Bosboom et al., 2014c, and references therein).

3.5. Anisotropy of Magnetic Susceptibility

In weakly deformed sediments, the analysis of the anisotropy of magnetic susceptibility (AMS) usually reflects the regional stress field and therefore enables the identification of the postdepositional tectonic regime (Tarling & Hrouda, 1993). From the Aertashi section, 345 samples were selected for AMS analysis at regular intervals throughout the section (the lowermost 82 samples from level 0 up to the base of unit A were collected by Bosboom et al., 2014a). This analysis was conducted using a KLY3-CS Kappabridge instrument. For each sample, we obtained principal susceptibility axes (K_{max}, K_{int}, and K_{min}), used to infer the fabric variations throughout the section (Figures 5 and S6 and Table S4). After tilt correction, we corrected the AMS directions for the observed vertical-axis rotation recorded above to determine the original anisotropy orientations.

The degree of anisotropy is relatively high, consistent with the magnetic mineralogy dominated by hematite. The minimum anisotropy axes (K_{min}) observed throughout the section are nearly vertical in tilt-corrected coordinates, indicating a clear sedimentary fabric obtained in response to gravity strain acquired at or near the time of deposition. However, after correction of bedding tilt and of vertical-axis rotations, the magnetic lineation (K_{max}) aligns broadly in an E-W direction between 41.0 and 17.4 Ma and in the uppermost unit E between 17.4 and 15.0 Ma, the magnetic lineation shifts to roughly N-S (Figure 5).

Early laboratory depositional experiments indicated a link between anisotropy shape and sediment transport directions (Rees, 1965). However, in most tectonic belts, anisotropy of low field magnetic susceptibility of sedimentary rocks displays triaxial AMS ellipsoids mainly controlled by compaction and tectonic strain (Borradaile & Henry, 1997). Upon deformation, the lineation K_{max} quickly aligns perpendicular to the direction of maximum compression. A lineation perpendicular to the compressional direction is typically acquired during the early stages of diagenesis and deformation (Frizon de Lamotte et al., 2002; Parés et al., 1999). The magnetic lineation, usually known as layer-parallel shortening, develops parallel to fold axes and thus perpendicular to the principal strain direction (Kissel et al., 1986; Poblete et al., 2014; Robion et al., 1995; Roperch et al., 2010; Sagnotti & Winkler, 1999; Soto et al., 2009). If not reset by strong subsequent deformation, the initial layer-parallel shortening of this early acquired magnetic fabric usually behaves as a passive marker recording early deformation and subsequent tectonic rotations (Roperch et al., 2011). This results in a hybrid triaxial fabric with the K_{min} perpendicular to bedding as observed in the Aertashi sediments. The striking change from E-W magnetic lineation through the section (41.0–17.4 Ma) to perpendicular N-S lineation in the uppermost unit (17.4–15.0 Ma) is therefore interpreted to reflect a change in principal strain direction from N-S to E-W affecting only the upper strata deposited after 17.4 Ma (Figure 5). The fabric must have been acquired after sufficient sediment has been deposited to be affected by tectonic strain, but before the bedding has been tilted.

3.6. εNd Analysis

The Sm-Nd values of a mudstone largely reflect its provenance (ancient crustal rocks have more negative ƐNd values, while juvenile mafic rocks have more positive ƐNd values). In this paper, we use this technique to build upon previous research carried out by Blayney et al. (2016), interpreting shifts in εNd values and hence provenance in terms of tectonics. In light of the previous data, a further 11 mudstone samples were added to the previous data set to more tightly constrain the previously identified timing of shifts in eps Nd values, now also aided by our own magnetostratigraphic data to more accurately place and thus date the samples. A shift to more negative, crustal, εNd values is seen starting at the base of unit D, immediately after the hiatus in the section and dated at 21.6 Ma (Figure 5). A second major shift, to more juvenile, less negative values, is seen at the top of unit E ~15.0 Ma.

Table 1
Stratigraphic Nomenclatures From This and Other Studies Compiled

Age (Ma)	Aertashi	Aertashi	Aertashi	Map J43C004003	Sanju	Kekeya	Western Tarim	Mine (Ulugqat)	Kashi basin
15–11	Unit F	Xiyu[a]	N.A.	Upper Wuqia (N1 W2)	Xiyu[a]	Xiyu[a]	Xiyu[a]	Xiyu[a]	Xiyu[a]
18.1–17.4	Unit E	Atux	N.A.	Upper Wuqia (N1 W2)	Atux	Atux	Pakabulake	Pakabulake	Atux
21.6–18.1	Unit D	Atux	N.A.	Lower Wuqia (N1 W1)	Not exposed	Atux	Pakabulake	Anjuan	Atux
27.4–24.3	Unit C	Wuqia undif.	N.A.	Bashibulake[a] (E2-3b)	Not exposed	Wuqia undif.	Anjuan	Keziluoyi	Pakabulake
32.2–27.4	Unit B	Wuqia undif.	Wuqia undif.	Bashibulake[a] (E2-3b)	Not exposed	Wuqia undif.	Keziluoyi	Hiatus	Unit C
33.0–32.2	Unit A	Wuqia undif.	Wuqia undif.	Bashibulake[a] (E2-3b)	Not exposed	Wuqia undif.	Keziluoyi	Hiatus	Units A and B
41–35.6	Bashibulake[o]	Bashibulake[o]	Keziluoyi	Bashibulake[a] (E2-3b)	Not exposed	Keziluoyi	Bashibulake[o]	Bashibulake[a]	Units A and B
Reference	*This study*	Zheng et al. (2015a, 2015b)	(Bosboom et al., 2014b)	Cao et al. (2015)	Zheng et al. (2015a, 2015b)	Wei et al. (2013)	Wang and Peng (2013)	Yang et al. (2014)	Heermance et al. (2007)

[a]Time-transgressive diachronous deposition from 20 to 5 Ma. Marine in the northwestern Tarim and continental in southwestern Tarim.

4. Discussion

4.1. Regional Stratigraphy of Western Tarim

4.1.1. Correlation of Defined Stratigraphic Units to Regional Formations

As part of our review of Western Tarim stratigraphy, we first clarify the nomenclature of the studied formations (Table 1). The termination of the last marine incursion at Aertashi is recorded in the Wulagen formation, recognized by diagnostic marine fossil assemblages (Bosboom et al., 2014b). The overlying unit is composed of continental fluvial red beds and extends from 41.0 to 35.6 Ma based on magnetostratigraphy (Bosboom et al., 2014a). As such it is time equivalent to the Bashibulake formation defined in the northwest Tarim basin where it is an alternation of marine and nonmarine deposits (e.g., Hao & Zeng, 1984; Sobel, 1995). However, the marine incursions of the Bashibulake formation in northwest Tarim did not reach as far south as the Aertashi region, where time-equivalent deposits are exclusively continental (Bosboom et al., 2014a). At Aertashi, this unit has thus been assigned either to the Bashibulake formation by Zheng et al. (2015a), Yin et al. (2002) or the Keziluoyi formation by Bosboom et al., (2014a). We here attribute this unit to the *nonmarine time equivalent of the Bashibulake formation* defined in northwest Tarim.

The top of this basal continental unit is marked by a facies change to coarser lithologies associated with the depositional hiatus from 35.6 to 33.0 Ma. The overlying A, B, and C units are assigned to the Keziluoyi, Anjuan, and Pakabulake formations, respectively, and units D and E are assigned to the Artushi (also known as the Atux) formation. Note that this assignment of units D and E follows Zheng et al. (2015a); it is different to Wei et al. (2013), which assigns units D and E to the Pakabulake formation. Overlying the Artushi formation are the extensive conglomerates of unit F assigned to the Xiyu formation as described by Zheng et al. (2015a) but different to the regional geologic map (Wang & Peng, 2013) where this conglomeratic formation is labeled as Upper Wuqia Group (N1 W2), actually below the Atux formation (N2a) and Xiyu formation QP1x.

4.1.2. Comparison to Western Tarim Magnetostratigraphy Studies

Several Cenozoic sections along the western margin of the Tarim basin have been dated using magnetostratigraphy with variable reliability (see Figures 1 and 6 for locations). The best dated and most complete section is clearly the Aertashi section reported here. It therefore constitutes a reference section to which the others can be compared.

1. *Southwestern Tarim*. At the *Kekeya* section (Figure 7), the first magnetostratigraphic dating of this section by Zheng et al. (2000) was shown to be much older in Zheng et al. (2015a) due to the discovery of an ash layer in the section that required recalibration of the magnetostratigraphy. Zheng et al. (2015a) proposed two alternative magnetostratigraphic correlations: one which they proposed fits the magnetostratigraphic data better, the other which they proposed fits the stratigraphic correlation better. They chose the latter as their preferred correlation assuming that the onset of Xiyu formation conglomerates, well dated at Aertashi at 15 Ma, must be contemporaneous with the Xiyu conglomeratic onset at Kekeya. However, given that the Xiyu conglomerates have been shown to be extremely diachronous (e.g., Charreau et al., 2009; Heermance et al., 2008), and that the Xiyu conglomerates at Aertashi are derived from the Pamir to the west (Blayney et al., 2016), it seems unlikely that the Xiyu formation at these two locations, affected by different tectonic regimes at that time, is coeval. We therefore used the first correlation of Zheng et al. (2015a), which is stronger in terms

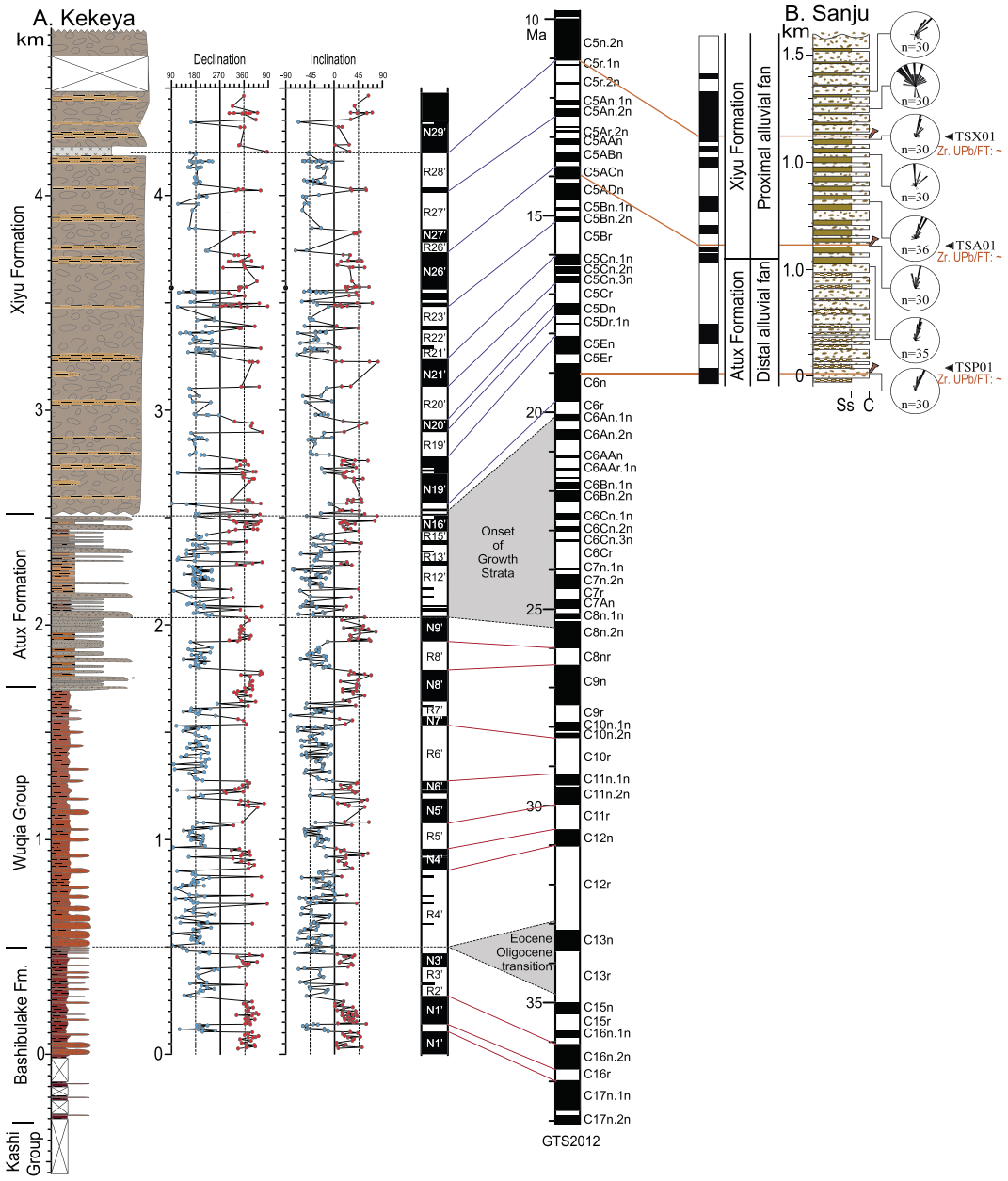

Figure 7. (a) Alternative magnetostratigraphic correlations of the Kekeya section (see Zheng et al. (2015a, 2015b) for legend and caption on original figure and paleomagnetic results) indicated by blue and red lines modified from the two originally proposed correlations by Zheng et al. (2015a, 2015b). The correlation proposed here (see text) identifies an interval within 25–20 Ma of discontinuous accumulation (shaded grey) corresponding to the onset of growth strata at the nearby Qipang section (Wang & Wang, 2016). Further slight modifications have been made to the correlation to fit the onset of coarser grained deposits with depositional hiatus at the Eocene-Oligocene transition, at the onset of growth strata (25.4 Ma) and the onset of the Xiyu conglomerate (20.2 Ma). (b) Age constraints of the Sanju section (see Cao et al., 2015 for legend and caption on original figure) and its correlation to the Kekeya section.

of correlations of observed polarity zones to the GPTS for the upper part of the section, to propose yet another alternative correlation. This correlation fits much better with the record of the nearby Sanju section that also shows conglomeratic deposition starting as early as 20 Ma (Cao et al., 2015 and see Sanju section below). In addition, using this correlation identifies an interval of discontinuous deposition from 25 to 20 Ma (see Figure 7) that likely represents the expression of the onset of growth strata documented in the nearby Qipan seismic section in the same stratigraphic interval (Wang & Wang, 2016).

At the Sanju section, Sun and Liu (2006) provided a very young Pliocene age based on magnetostratigraphy for the mostly conglomeratic deposits in this section. However, these ages have been revised by Cao et al. (2015) to be much older (from circa 19 Ma at the base of the section to circa 11 Ma 1 km stratigraphically above, Figure 7), based on double U-Pb and fission track dating of detrital zircon. These new ages imply that the Sanju conglomeratic section is coeval to the conglomerates in the Kekeya section starting circa 20 Ma. The onset of conglomeratic deposition is actually not exposed in the Sanju section and must occur below the circa 19 Ma base of the section. A change from distal to proximal alluvial fan is reported just below a sample dated circa 14 Ma.

2. *Northwestern Tarim*. Yang et al. (2014) report a reliable magnetostratigraphy partly constrained by detrital AFT ages from the *Mine* (*Ulugqat*) section: The onset of continental clastic deposition is found at 20.8 Ma above a very large hiatus on the marine Priabonian Bashibulake formation. This study also reports a depositional onset of coarse clastics and conglomerates between 15 and 14 Ma. Provenance from the Tian Shan to the north is indicated by detrital Zr U-Pb age distributions (Yang et al., 2014). This is in good agreement with the magnetostratigraphic results from the *Kashi foreland basin* further east along the southern margin of the Tian Shan (Heermance et al., 2007, 2008). Multiple magnetostratigraphic sections from the Kashi foreland basin indicate that the time-transgressive Xiyu conglomerate has prograded south since just after initial uplift at circa 20 Ma and intensified circa 15 Ma.

Other magnetostratigraphic results have been reported from Western Tarim, in particular at Keliyang (Sun et al., 2016), from the Maza Tagh (Sun et al., 2009) or at Oytag (Sun & Jiang, 2013, Figure 1) but we prefer to omit reinterpreting them here because we have not been able to make satisfactory stratigraphic correlations due to insufficient data reliability, the lack of acceptable magnetostratigraphic correlations based on unambiguous biostratigraphic and independent constraints, and/or insufficiently described lithologies.

This compilation and reinterpretation of stratigraphic records highlight, at around 25–20 Ma, the occurrence of growth strata and conglomerates in the south (Aertashi, Kekeya, and Sanju sections) and the onset of deposition in the north (Kashi basin and Mine sections). This suggests tectonic activity starting around 25–20 Ma followed by time transgressive propagation into Tarim and a resurgence of regional subsidence circa 15 Ma as previously documented for northern Tarim and around the Tian Shan range (e.g., Charreau et al., 2009; Heermance et al., 2008).

4.2. Tectonic Rotation

The distribution of vertical-axis rotations expected from various models of indentation of the Pamir salient has been described by Cowgill (2010). Accordingly, indentation is associated with rotations when accommodated by radial thrusting or oroclinal bending (or buckling). Indentation is mostly nonrotational if accommodated by transfer faulting, in which strike-slip faulting on the sides of the salient accommodates the indentation. In this case, however, strike-slip motion may induce vertical-axis rotations concentrated along the fault due to shear and associated drag folding and rotation of thrust wedges (Dupont-Nivet et al., 2002). Based on the observations that counterclockwise rotations are large (20 to 40°) and pervasive west of the Pamir in Cretaceous to Miocene sediment of the Afghan-Tajik basin (Bourgeois et al., 1997; Thomas et al., 1996) but that clockwise rotations were not recorded to the east in Tarim, Cowgill (2010) proposed a model in which Pamir indentation has been accommodated by radial thrusting to the west and transfer faulting to the east. However, Bosboom et al. (2014c) later reported results showing systematic clockwise rotations at the Aertashi and Kezi (near Qimugen) sections that seemingly ceased by the end of the Oligocene. On this basis, those authors supported the model of Cowgill (2010) for the evolution of the Pamir salient but from Miocene times onward, counterclockwise rotation continued in the Tajik basin but ceased in the Tarim basin. Cessation of rotation in the Tarim basin was interpreted to be the result of the onset of movement on the KYTS, and thus transfer of movement to indentation, facilitated by dextral strike-slip motion along the eastern margin (with limited distributed shear).

Our new data, however, indicate that most of the rotation occurred sometime after 15.0 Ma, with a small amount prior to this time. This 15.0-Ma age also corresponds to the time when the east-propagating QFTS (Figure 1), which includes the Aertashi study area, became active based on growth strata in the Xiyu formation now dated by our study at 15 Ma (Wang & Wang, 2016; Wei et al., 2013). This suggests that before that time, the study area, lying within the footwall in the Tarim basin, was only slightly affected by the rotation. It is only when the study area became part of the QFTS that it rotated clockwise, coinciding with the timing of

the change to Pamir provenance at 15.0 Ma, and associated dextral shear along the KYTS affecting the thrust sheets.

We note that part of the observed clockwise rotation documented at Aertashi may relate to wholesale clockwise rotation of the Tarim basin in addition to local processes. In favor of wholesale Tarim rotation, previous paleomagnetic studies from the nearby Qimugen section, and also from central and southern Tarim, have consistently documented ~15° clockwise rotation in loosely dated Miocene sediments (Dupont-Nivet et al., 2002, Gilder et al., 2001 and a regional review in Bosboom et al., 2014c). Furthermore, based on geometric considerations, Avouac et al. (1993) first estimated a maximum 7.0 ± 0.25° of clockwise rotation of the Tarim basin about an axis at the eastern end of the basin (96°E; 43.5°N) that would explain the shortening in the Tian Shan increasing to circa 200 ± 50 km at the western end of the Tarim basin (see also Van Hinsbergen et al., 2011). This has been substantiated by Global Positioning System measurements indicating present clockwise rotation of the Tarim basin about an axis at its eastern end at rates of 11 ± 1 nrad/year (Shen et al., 2001) or 0.6 ± 0.06°/Myr assuming this rate has been steady and can be extrapolated far back in time. At this rate, it would take at least about 12 Myrs for Tarim to rotate 7°. Confirming wholesale rotation will require extensive paleomagnetic data regionally distributed over Tarim. In any case, although some of the 15° clockwise rotation recorded at Aertashi may have been accommodated by wholesale Tarim rotation, a significant part of the observed rotation must be associated with local structures such as the QFTS activity after 15 Ma.

4.3. Synthesis of Basin Evolution

4.3.1. 41.0–24.3 Ma: Distal Foreland Basin

The depositional environments shift at 41.0 Ma from shallow marine to continental deposits with an increase in tectonic subsidence. From then on until 24.3 Ma, the section is characterized by no significant change in depositional environment, accumulation rate, sediment source, or strain direction. Sediment source is from the distant Kunlun including the Songpan-Ganzi further south within the Tibetan Plateau (Blayney et al., 2016). The strain direction from AMS is consistent with N-S compression.

The marine to continental facies change has previously been explained as a combination of eustatic sea level fall and basin infilling due to increased tectonic activity (Bosboom et al., 2014a). The dramatic increase of tectonic subsidence at 41 Ma, followed by its continued increase, favors the proposal that subsidence is predominantly the result of the tectonism. Also, no global sea level fall is associated to this period that could explain the regression (Gasson et al., 2012). The combination of a regression with increased subsidence is interpreted to result from increased basin infilling overcompensating the subsidence and resulting in the marine to continental transition.

4.3.2. 24.3–21.6 Ma: Northward Propagation of Deformation to Aertashi

A depositional hiatus (24.3–21.6 Ma) is recorded in the Aertashi section, associated with a change from distal foreland basin deposits below to proximal conglomerates at the toe of an alluvial fan. The conglomerates deposited above the hiatus from 21.6 to 18.2 Ma fine upward and are composed predominantly of sedimentary clasts, thus requiring a proximal source with relatively little exhumation. Our updated Sm-Nd record (Figure 5) allows us to constrain the timing of the shift in ℇNd values more precisely compared to Blayney et al. (2016). It occurs just above the disconformity at 21.6 Ma.

This hiatus and change in facies and provenance is synchronous with exhumation recorded by AFT ages from lower Cretaceous strata at the base of the Aertashi section a few kilometers to the west (Sobel & Dumitru, 1997). Therefore, the 2.3-Myr-long disconformity (24.3–21.6 Ma) is most likely linked to this coeval exhumation with the AFT data indicating a minimum age of 20.0 ± 3.1 Ma for the time of cooling below 120–100 °C (Sobel & Dumitru, 1997). According to Sobel and Dumitru (1997), the partially annealed tracks and nonuniform age distribution indicates that the grains have been nearly but not fully reset and are therefore interpreted to have resided near the minimum 120–100 °C track annealing temperature before exhumation. Seven samples analyzed by Sobel and Dumitru (1997) from younger stratigraphic levels experienced progressively less annealing. This exhumation from shallow depth is supported by the composition of the overlying conglomerate clasts in unit D, composed principally of shallow cover deposits (mainly sandstones and limestone), indicating little unroofing. This exhumation is also consistent with the ~2-km stratigraphic thickness measured between the marine limestone deposits and the disconformity (Figures 5 and 8. Within the Aertashi section, the depositional hiatus can be estimated to represent about 400 m of

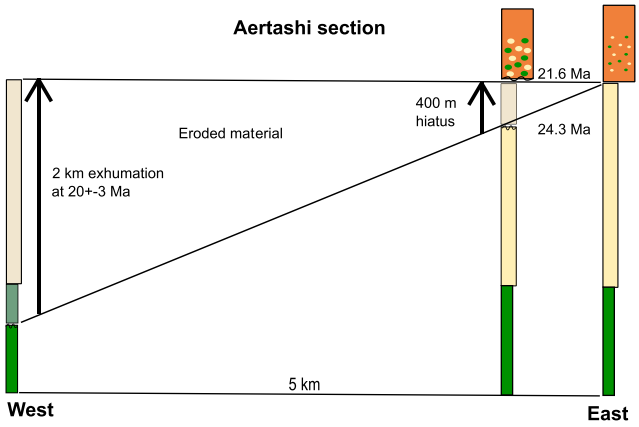

Figure 8. Sketch illustrating diminishing exhumation/erosion from west to east along the Aertashi section. Three columns depict schematic stratigraphic sections before the exhumation/erosion event with Cretaceous (green), Cenozoic up to 21.6 Ma (beige), and above 21.6 Ma (orange with clasts from reworked underlying sediments). Shaded areas depict eroded portions of the stratigraphy. The left column is at the site of maximum exhumation determined from apatite fission track data (Sobel & Dumitru, 1997). The middle column is at the location of the 400-m hiatus within the sampled Aertashi section. The right column locates at the hypothesized continuation basinward where the deposition may have been continuous without hiatus.

sediment lacking given the measured accumulation rate of 150 m/Myr (Figure 8). The combination of the documented nearby exhumation to the west and the hiatus overlain by the onset of conglomeratic deposition together indicates a proximal tectonic structure uplifted to the west of the study site in this 24.3- to 21.6-Ma period (Figure 9b).

4.3.3. 21.6–15.0 Ma: Transtensional Basin Along the KYTS

After the hiatus, conglomerates grade into a thick sequence of fine sediments that accumulated until 15.0 Ma. From 18.2 to 15.0 Ma, fining upward clastics accumulated at Aertashi with drastically increasing rates and an upward evolution from debris flow dominated proximal alluvial fan deposits to fine-grained, muddy floodplain of distal alluvial fan deposits. Despite the nearby structural activity described above, the grain size decreases and the source remains similar in this interval with no sign of contribution from the Pamir or deeper crustal levels. This suggests that the nearby structure at Aertashi did not evolve into a thrust belt propagating eastward during this time interval, or the section would have recorded a coarsening upward succession, being overthrust by structurally deeper basement and/or fully exhumed. The continuously increasing accumulation of fining upward clastics near to the site of exhumation, the observation that only surficial sedimentary cover has been exhumed, and the absence of eastward propagation into the basin more likely indicate that the structure is mainly strike slip, possibly with an extensional component. This hypothesis of a transtensional setting is supported by the previously reported synchronous circa 20 Ma exhumation at two locations (Kulisaf and Aertashi) along the dextral strike-slip KYTS (Sobel & Dumitru, 1997), by reported ductile shearing along the westernmost strand of the KYTS (Cai et al., 2017), and by the reported strike-slip negative flower structure in the Tarim subsurface (Wei et al., 2013). Based on these structures, Bande et al. (2015)

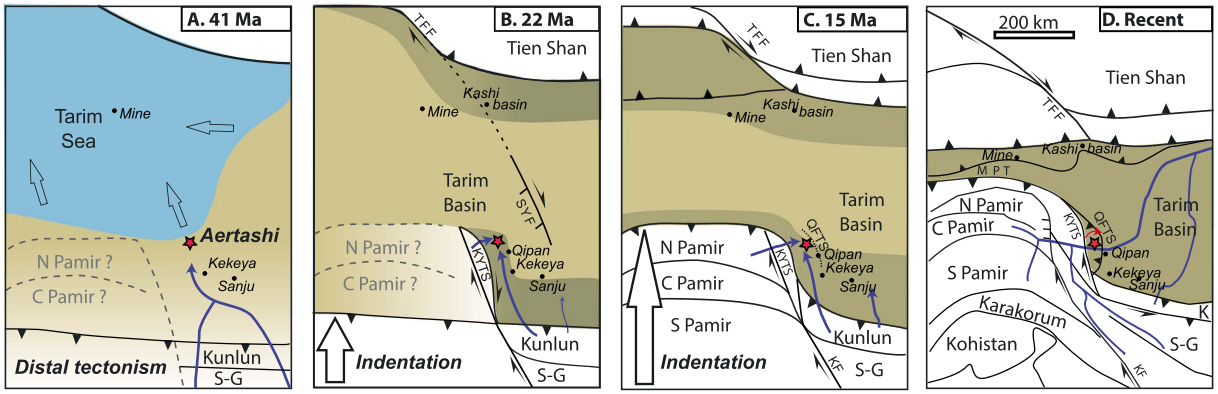

Figure 9. Schematic evolution of the Pamir salient interpreted from the sedimentary record at Aertashi (red star) and other sections (black dots, see part 4.1 for review). Uplifted areas are depicted in white. Marine and continental basins are depicted blue and yellow, respectively, with darker yellow areas indicating coarse clastics (e.g., conglomerates). Schematic paleodrainage patterns are illustrated by blue lines. A total of about 300 km of Pamir indentation and 200 km of Tian Shan-Tarim shortening is illustrated with the Tarim basin used as fixed reference. Large open arrows indicate the direction of *indentation* that refers either to the northward penetration of the Pamir terranes overthrusting Tarim (*subduction model*) or to the northward penetration of mantle lithosphere below the crust (delamination models, see text). In Figures 9a and 9b, the Pamir terranes are depicted with dashed lines and question marks to indicate that they have either not yet indented into Tarim according to the subduction model or are already present according to the delamination models. (a) At 41 Ma, the Tarim sea retreat and the onset of subsidence are related to distal tectonic activity to the south. (b) At 22 Ma, regional deformation activates Tien Shan and Kunlun thrusting over Tarim. The KYTS initiation, ahead of the indentation in south Tarim, is expressed by local deformation and uplift contributing conglomerates to Aertashi. The KYTS interaction with the SYF possibly formed a transtentional setting. (c) At 15 Ma, the indentation reaches the vicinity of Aertashi where the west vergent QTFS activates and proximal sediments from North Pamir are deposited. (d) From 15 Ma to recent, Pamir indentation into Tarim is accommodated by the MPT while Tien Shan overthrusting increases. The QFTS rotates clockwise. The catchment area of the Aertashi River reaches to the Central Pamir, South Pamir, and further. S-G = Songpan-Ganzi terrane; K = Kunlun terrane; KYTS = Kashgar-Yecheng Transfer System, SYF = Shache-Yangdaman fault, TFF = Talas-Fergana fault, MPT = Main Pamir Thrust, PFT = Pamir Frontal Thrust, QFTS = Qimugen Frontal Thrust System, KF = Karakorum fault.

proposed a pull apart basin for the region, bounded by the KYTS along the western margin and the SYF to the east, which is proposed to represent a southern continuation of the Talas Fergana fault (Figure 9b).

More regionally, reconstructed isopach maps of formations corresponding to this 21.6- to 15.0-Ma interval (Wei et al., 2013) indicate that the Tarim depocenter was located around the Aertashi-Qimugen area toward the middle of the western Tarim margin at this time (note that this takes into account our stratigraphic formation assignments from section 4.1 above, where the Anjuan formation in Figure 6d of Wei et al. is interpreted as the Pakabulake formation in this study and the Pakabulake formation in Figure 6e is interpreted as the Atux formation in this study). In the same 21.6- to 15.0-Ma time interval, mostly conglomerates were deposited along the southern margin of Tarim, derived from exhumation associated with northward thrusting of the Kunlun hinterland (e.g., Cheng et al., 2017). In that area, growth strata formed at circa 25–20 Ma based on seismic investigations at the Qipan seismic section further south along the KYTS (Figure 9b, Wang & Wang, 2016). These growth strata are directly followed by the onset of conglomeratic deposits starting around 20 Ma as indicated by dating at the nearby Kekeya stratigraphic section (Cao et al., 2015, see section 4.1 above, Figure 7). To the north along the north-western Tarim margin, increasing accumulation rates and southward propagation of conglomerates suggest southward migrating foreland deformation since circa 20 Ma, associated with continuing exhumation of the southwestern Tian Shan (Heermance et al., 2008; Yang et al., 2015). We therefore consider that the increasing subsidence and accumulation at Aertashi from 21.6 to 15.0 Ma may be related to a combination of regional loading and overthrusting by the Tarim basin margins with the nearby strike-slip structure also influencing the location of the depocenter, the local stress field, and the accumulation rates (Figure 9b).

4.3.4. 15 Ma to Recent: Pamir Indentation Reaches and Exceeds the Latitude of Aertashi

At 15.0 Ma, a major shift to proximal alluvial fans composed of boulder conglomerate is recorded, with a shift to provenance from the North Pamir (Blayney et al., 2016). Between 15.0 and circa 11 Ma, dominantly conglomeratic deposits continue to be accumulated at high rates. The occurrence of fresh volcanic detritus (Blayney et al., 2016) at 11 Ma in the Aertashi record corresponds to the age of the 11-Ma Dunkeldik volcanics providing a likely source from the Central Pamir terrane (Hacker et al., 2005; Kooijman et al., 2017; Wei et al., 2018). This age range also corresponds to the clockwise rotation (see above) and the suggested onset of QFTS (Wei et al., 2013, Figure 9c). Together, this indicates that the tectonic setting changed drastically at 15 Ma in response to east verging thrusting of the Pamir onto Tarim. This change in tectonic setting is consistent with the N-S to E-W shift in maximum strain orientation recorded by AMS data in post-17.4-Ma sediments. The acquisition of this E-W strain fabric affecting the approximately 1-km-thick fine clastics deposited between 17.4 and 15.0 Ma, likely occurred during the post-15-Ma east vergent tectonic event. This change of tectonic setting and provenance at 15 Ma provides important kinematic constraints on the timing and position of the Pamir indentation into Tarim discussed below.

4.4. Tectonic Implications

4.4.1. 41.0–24.3 Ma

Our data together with provenance data from Blayney et al. (2016) suggest a distal foreland basin environment (Figure 9a) that can be linked to the south with the Kunlun—a topographic feature likely elevated since ~200 Ma—and further south with the northern Qiangtang/Central Pamir (Cao et al., 2014; Rutte, Ratschbacher, Schneider, et al., 2017). This is consistent with well-established regional tectonism, and associated magmatism at ~50–40 Ma is in the Songpan-Ganzi and Qiangtang terranes of Tibet as well as the South and Central Pamir terranes (e.g., Chapman et al., 2017, 2018; Rohrmann et al., 2012; Rutte, Ratschbacher, Schneider, et al., 2017; Staisch et al., 2016; Stübner, Ratschbacher, Weise, et al., 2013; Wang et al., 2008; Zhao et al., 2016).

4.4.2. 24.3–21.6 Ma

At 24.3–21.6 Ma, our results show deformation along the southern Tarim margin and propagation of deformation along the western margin of Tarim, coeval with uplift in the Kunlun and Tian Shan, indicating a major regional change in geodynamic settings (Figure 9b). The resurgence of deformation propagating northward into Tarim at 24.3–21.6 Ma indicated by our results is in agreement with models allowing for indentation at this time in response to either intracontinental subduction (Sobel et al., 2013) or Pamir lithosphere (Chapman et al., 2017). However, our results are at odds with models implying that the indentation started much later (e.g., Küfner et al., 2016). Additionally, provenance results show no evidence for Pamir sources at Aertashi before 15.0 Ma despite the occurrence of proximal conglomerates since 21.6 Ma. This

suggests Pamir terranes were not adjacent to Aertashi but further south as implied by the continental subduction model (Figure 9b). Alternatively, the Pamir terranes may have been adjacent but not yet drained by the river system flowing to Aertashi or not exhumed sufficiently to be expressed in the Aertashi detritus that consists mainly of reworked sedimentary cover. In either case, our results suggest that the Pamir indentation had not yet reached Aertashi.

4.4.3. 15–0 Ma

From 15 Ma onward, the Pamir indentation and uplift had reached the vicinity of the study area recording proximal conglomerates of the Northern Pamir by 15 Ma and Central Pamir terrane by 11 Ma (Figures 9c and 9d). In the Pamir as well as Tian Shan, this period corresponds to resumed shortening and exhumation (e.g., Charreau et al., 2009; Rutte, Ratschbacher, Khan, et al., 2017). The resumption of crustal thickening at this time has been interpreted, in the subduction model of Sobel et al. (2013), to a change in the degree of coupling between the downgoing and overriding slab resulting in renewed crustal thickening. In the delamination models (Chapman et al., 2017; Küfner et al., 2016), the 300-km Pamir indentation into Tarim would start in South Pamir only at 10 Ma and reach the present position of Aertashi only around 5 Ma, based on retro-positioning the northern edge of the Indian lithospheric indenter using the Indian plate motion (Molnar & Stock, 2009; note that the position of the Indian indenter appears to have been miscalculated in Chapman et al., 2017 to be at 25–20 Ma, 100–125 km south of its present position instead of 1,000–1,250 km). However, our data imply that the northward propagation of deformation was already underway by 24.3–21.6 Ma in south Tarim, with at least half of the 300 km consumed when the northern Pamir reached the latitude of Aertashi at 15 Ma. In addition, in the delamination models a large part of the Pamir indentation into Tarim remains to be accommodated after 5 Ma but the slip on the KYTS appears to have mostly stopped by about 5–3 Ma (Ischuk et al., 2013; Sobel et al., 2011; Zubovich et al., 2016).

Our results constraining the timing of the northward propagation of deformation into Tarim are more consistent with the intracontinental subduction end-member model, although it does not solve the inherent problem that this model requires accommodating the 300 km indentation by the limited northward crustal shortening that is documented along the Pamir (see Chapman et al., 2017 for further discussion). A potential solution may involve ~200 km of delamination-driven indentation starting circa 25–20 Ma and progressing northward under the preexisting Pamir salient to reach Aertashi at 15 Ma with limited shortening, followed by ~100 km of northward overthrusting to reach a near modern configuration around 5 Ma. However, additional work is needed to provide evidence for such a model.

5. Conclusions

Our magnetostratigraphic, sedimentologic, and provenance results from the Aertashi section of western Tarim provide a sedimentary record of Pamir deformation, revealing the following sequence of tectonic events. (1) 41–24.3 Ma; a marine to continental facies transition and increased clastic sediment accumulation are related to increased tectonic activity. This is interpreted as a distal foreland basin response to crustal thickening in northern Tibet and Pamir further south. (2) 24.3–21.6 Ma; a depositional hiatus and subsequent first influx of conglomerates at Aertashi are related to nearby exhumation of the sedimentary cover. This is interpreted as the propagation of the KYTS strike-slip system to the Aertashi area. (3) 21.6–15.0 Ma; fining upward proximal to distal sequences with increasing accumulation rates indicate increasing tectonic subsidence in the Aertashi region, which constitutes by this time the southwest Tarim basin depocenter. This is interpreted as a response to the combination of dextral transtensional deformation along the western margin of Tarim with regional deformation from thrust loading from the Kunlun. (4) 15.0 - Recent; proximal alluvial fan conglomerates sourced from the North Pamir appear at 15.0 Ma in Aertashi, followed by diagnostic volcanics from the Central Pamir at 11 Ma. A 14° clockwise rotation is associated with the activation of the east verging QFTS and a strain orientation shifting from N-S to E-W. This together suggests that Pamir indentation had reached Aertashi no later than 15.0 Ma.

Acknowledgments

Data used for this paper are available in the supporting information section, Tables S4 and S5, and the database that contains paleomagnetic diagrams for each sample. This work was funded by a NERC PhD Studentship to Blayney (grant NE K501001-1) and by a VIDI grant from the Netherlands Organization for Scientific research (NWO), an ERC consolidator grant MAGIC, ANR DSP-Tibet, and support from the Alexander von Humboldt to Dupont-Nivet. We would like to thank Douwe van Hinsbergen and Roberto Molina for constructive reviews; Annabelle Bernard, Laura Fielding, Chris Kneale, and our guides Kasim and Khader for their contributions in the field; and Guangsheng Zhuang for his considerable efforts in getting our samples safely back to the UK. We thank Sofia Küfner for discussions.

References

Avouac, J. P., Tapponnier, P., Bai, M., You, H., & Wang, G. (1993). Active thrusting and folding along the northern Tien Shan and Late Cenozoic rotation of the Tarim relative to Dzungaria and Kazakhstan. *Journal of Geophysical Research*, *98*(B4), 6755–6804. https://doi.org/10.1029/92JB01963

Bande, A., Sobel, E. R., Mikolaichuk, A., & Acosta, V. T. (2015). Talas–Fergana fault Cenozoic timing of deformation and its relation to Pamir indentation. *Geological Society, London, Special Publications*, *427*, SP427. 421.

Bird, P. (1979). Continental delamination and the Colorado plateau. *Journal of Geophysical Research*, *84*(B13), 7561–7571.
Blayney, T., Najman, Y., Dupont-Nivet, G., Carter, A., Millar, I., Garzanti, E., & Vezzoli, G. (2016). Indentation of the Pamirs with respect to the northern margin of Tibet: Constraints from the Tarim basin sedimentary record. *Tectonics*, *35*, 2345–2369. https://doi.org/10.1002/2016TC004222
Borradaile, G., & Henry, B. (1997). Tectonic applications of magnetic susceptibility and its anisotropy. *Earth-Science Reviews*, *42*(1), 49–93.
Bosboom, R., Dupont-Nivet, G., Grothe, A., Brinkhuis, H., Villa, G., Mandic, O., & Guo, Z. (2014a). Linking Tarim basin sea retreat (west China) and Asian aridification in the Late Eocene. *Basin Research*, *26*, 621–640. https://doi.org/10.1111/bre.12054
Bosboom, R., Dupont-Nivet, G., Grothe, A., Brinkhuis, H., Villa, G., Mandic, O., & Yang, W. (2014b). Timing, cause and impact of the late Eocene stepwise sea retreat from the Tarim basin (west China). *Palaeogeography, Palaeoclimatology, Palaeoecology*, *403*, 101–118.
Bosboom, R., Dupont-Nivet, G., Huang, W., Yang, W., & Guo, Z. (2014c). Oligocene clockwise rotations along the eastern Pamir: Tectonic and paleogeographic implications. *Tectonics*, *33*, 53–66. https://doi.org/10.1002/2013TC003388
Bosboom, R. E., Dupont-Nivet, G., Houben, A. J. P., Brinkhuis, H., Villa, G., Mandic, O., & Krijgsman, W. (2011). Late Eocene sea retreat from the Tarim basin (west China) and concomitant Asian paleoenvironmental change. *Palaeogeography, Palaeoclimatology, Palaeoecology*, *299*(3–4), 385–398. https://doi.org/10.1016/j.palaeo.2010.11.019
Bourgeois, O., Cobbold, P. R., Rouby, D., Thomas, J. C., & Shein, V. (1997). Least squares restoration of Tertiary thrust sheets in map view, Tajik depression, central Asia. *Journal of Geophysical Research*, *102*(B12), 27,553–27,573.
Burtman, V., & Molnar, P. (1993). Geological and geophysical evidence for deep subduction of continental crust beneath the Pamir. *Geological Society of America Special Papers*, *281*(281), 76.
Butler, R. F. (1992). *Paleomagnetism: Magnetic domains to geologic terranes*. Boston: Blackwell Scientific Publications.
Cai, Z., Xu, Z., Cao, H., Robinson, A. C., Li, G., & Xu, X. (2017). Miocene exhumation of northeast Pamir: Deformation and geo/thermochronological evidence from western Muztaghata shear zone and Kuke ductile shear zone. *Journal of Structural Geology*, *102*, 130–146.
Cao, K., Wang, G.-C., Bernet, M., Beek, P. V. D., & Zhang, K.-X. (2015). Exhumation history of the West Kunlun Mountains, northwestern Tibet: Evidence for a long-lived, rejuvenated orogen. *Earth and Planetary Science Letters*, *432*, 391–403.
Cao, K., Xu, Y., Wang, G., Zhang, K., Van Der Beek, P., Jiao, Y., & Bershaw, J. (2014). Neogene source-to-sink relations between the Pamir and Tarim basin: Insights from stratigraphy, detrital zircon geochronology, and whole-rock geochemistry. *The Journal of Geology*, *122*(4), 433–454.
Cardozo, N. (2012). OSX backstrip.
Carrapa, B., Mustapha, F. S., Cosca, M., Gehrels, G., Schoenbohm, L. M., Sobel, E. R., & Goodman, P. (2014). Multisystem dating of modern river detritus from Tajikistan and China: Implications for crustal evolution and exhumation of the Pamir. *Lithosphere*, *6*(6), 443–455.
Caves, J. K., Winnick, M. J., Graham, S. A., Sjostrom, D. J., Mulch, A., & Chamberlain, C. P. (2015). Role of the westerlies in central Asia climate over the Cenozoic. *Earth and Planetary Science Letters*, *428*, 33–43. https://doi.org/10.1016/j.epsl.2015.07.023
Chapman, J. B., Carrapa, B., Ballato, P., DeCelles, P. G., Worthington, J., Oimahmadov, I., & Ketcham, R. (2017). Intracontinental subduction beneath the Pamir Mountains: Constraints from thermokinematic modeling of shortening in the Tajik fold-and-thrust belt. *GSA Bulletin*, *129*(11–12), 1450–1471.
Chapman, J. B., Scoggin, S. H., Kapp, P., Carrapa, B., Ducea, M. N., Worthington, J., & Gadoev, M. (2018). Mesozoic to Cenozoic magmatic history of the Pamir. *Earth and Planetary Science Letters*, *482*, 181–192.
Charreau, J., Gilder, S., Chen, Y., Dominguez, S., Avouac, J.-P., Sen, S., & Wang, W. (2006). Magnetostratigraphy of the Yaha section, Tarim basin (China): 11 Ma acceleration in erosion and uplift of the Tian Shan mountains. *Geology*, *34*(3), 181–184.
Charreau, J., Gumiaux, C., Avouac, J.-P., Augier, R., Chen, Y., Barrier, L., & Wang, Q. (2009). The Neogene Xiyu Formation, a diachronous prograding gravel wedge at front of the Tianshan: Climatic and tectonic implications. *Earth and Planetary Science Letters*, *287*(3), 298–310.
Cheng, X., Chen, H., Lin, X., Wu, L., & Gong, J. (2017). Geometry and kinematic evolution of the Hotan-Tiklik segment of the western Kunlun thrust belt: Constrained by structural analyses and apatite fission track thermochronology. *The Journal of Geology*, *125*(1), 65–82.
Cowgill, E. (2010). Cenozoic right-slip faulting along the eastern margin of the Pamir salient, northwestern China. *Geological Society of America Bulletin*, *122*(1–2), 145–161. https://doi.org/10.1130/B26520.1
Demarest, H. H. (1983). Error analysis for the determination of tectonic rotation from paleomagnetic data. *Journal of Geophysical Research*, *88*(B5), 4321–4328. https://doi.org/10.1029/JB088iB05p04321
Dupont-Nivet, G., Guo, Z., Butler, R. F., & Jia, C. (2002). Discordant paleomagnetic direction in Miocene rocks from the central Tarim basin: Evidence for local deformation and inclination shallowing. *Earth and Planetary Science Letters*, *199*(3–4), 473–482. https://doi.org/10.1016/S0012-821X(02)00566-6
Fisher, R. (1953). Dispersion on a sphere. *Proceedings of the Royal Society of London. Series A: Mathematical and Physical Sciences*, *217*(1130), 295–305.
Frizon de Lamotte, D., Souque, C., Grelaud, S., & Robion, P. (2002). Early record of tectonic magnetic fabric during inversion of a sedimentary basin. Short review and examples from the Corbières transfer zone (France). *Bulletin de la Société Géologique de France*, *173*(5), 461–469.
Gasson, E., Siddall, M., Lunt, D. J., Rackham, O. J. L., Lear, C. H., & Pollard, D. (2012). Exploring uncertainties in the relationship between temperature, ice volume, and sea level over the past 50 million years. *Reviews of Geophysics*, *50*, RG1005. https://doi.org/10.1029/2011RG000358
Gilder, S., Chen, Y., & Sen, S. (2001). Oligo-Miocene magnetostratigraphy and rock magnetism of the Xishuigou section, Subei (Gansu Province, western China) and implications for shallow inclinations in central Asia. *Journal of Geophysical Research*, *106*(B12), 30,505–30,521.
Hacker, B., Luffi, P., Lutkov, V., Minaev, V., Ratschbacher, L., Plank, T., & Metcalf, J. (2005). Near-ultrahigh pressure processing of continental crust: Miocene crustal xenoliths from the Pamir. *Journal of Petrology*, *46*(8), 1661–1687.
Hao, Y., & Zeng, X. (1984). On the evolution of the west Tarim gulf from Mesozoic to Cenozoic in terms of characteristics of foraminiferal fauna. *Acta Micropalaeontologica Sinica*, *1*(1), 1–13.
Heermance, R. V., Chen, J., Burbank, D. W., & Miao, J. (2008). Temporal constraints and pulsed Late Cenozoic deformation during the structural disruption of the active Kashi foreland, northwest China. *Tectonics*, *27*, TC6012. https://doi.org/10.1029/2007TC002226
Heermance, R. V., Chen, J., Burbank, D. W., & Wang, C. (2007). Chronology and tectonic controls of Late Tertiary deposition in the southwestern Tian Shan foreland, NW China. *Basin Research*, *19*(4), 599–632. https://doi.org/10.1111/j.1365-2117.2007.00339.x
Ischuk, A., Bendick, R., Rybin, A., Molnar, P., Khan, S. F., Kuzikov, S., & Schelochkov, G. (2013). Kinematics of the Pamir and Hindu Kush regions from GPS geodesy. *Journal of Geophysical Research: Solid Earth*, *118*, 2408–2416. https://doi.org/10.1002/jgrb.50185

Jia, C. (1997). *Tectonic characteristics and petroleum, Tarim basin, China*. Beijing: Petroleum Industry Press.
Käßner, A., Ratschbacher, L., Jonckheere, R., Enkelmann, E., Khan, J., Sonntag, B. L., & Oimahmadov, I. (2016). Cenozoic intracontinental deformation and exhumation at the northwestern tip of the India-Asia collision—Southwestern Tian Shan, Tajikistan, and Kyrgyzstan. *Tectonics*, *35*, 2171–2194. https://doi.org/10.1002/2015TC003897
Kirschvink, J. L. (1980). The least-squares line and plane and the analysis of palaeomagnetic data. *Geophysical Journal International*, *62*, 699–718.
Kissel, C., Barrier, E., Laj, C., & Lee, T. Q. (1986). Magnetic fabric in "undeformed" marine clays from compressional zones. *Tectonics*, *5*, 769–781.
Kooijman, E., Smit, M. A., Ratschbacher, L., & Kylander-Clark, A. R. (2017). A view into crustal evolution at mantle depths. *Earth and Planetary Science Letters*, *465*, 59–69.
Küfner, S.-K., Schurr, B., Sippl, C., Yuan, X., Ratschbacher, L., Ischuk, A., & Tilmann, F. (2016). Deep India meets deep Asia: Lithospheric indentation, delamination and break-off under Pamir and Hindu Kush (Central Asia). *Earth and Planetary Science Letters*, *435*, 171–184.
Lan, X., & Wei, J. (1995). *Late Cretaceous–Early Tertiary marine bivalve fauna from the western Tarim basin* (p. 212). Beijing: Chinese Science Pubilishing House.
Liu, D., Li, H., Sun, Z., Cao, Y., Wang, L., Pan, J., & Ye, X. (2017). Cenozoic episodic uplift and kinematic evolution between the Pamir and Southwestern Tien Shan. *Tectonophysics*.
Mao, S., & Norris, G. (1988). *Late Cretaceous-early Tertiary dinoflagellates and acritarchs from the Kashi area, Tarim basin, Xinjiang Province, China*. Beijing: Chinese Science House.
Miall, A. D. (1985). Architectural-element analysis: A new method of facies analysis applied to fluvial deposits. *Earth Science Reviews*, *22*(4), 261–308.
Molnar, P., & Stock, J. M. (2009). Slowing of India's convergence with Eurasia since 20 Ma and its implications for Tibetan mantle dynamics. *Tectonics*, *28*, TC3001. https://doi.org/10.1029/2008TC002271
Negredo, A. M., Replumaz, A., Villaseñor, A., & Guillot, S. (2007). Modeling the evolution of continental subduction processes in the Pamir–Hindu Kush region. *Earth and Planetary Science Letters*, *259*(1), 212–225.
Ogg, J. G., Ogg, G., & Gradstein, F. M. (2016). *A concise geologic time scale: 2016*. Amsterdam, Netherlands: Elsevier.
Parés, J. M., van der Pluijm, B. A., & Dinarès-Turell, J. (1999). Evolution of magnetic fabrics during incipient deformation of mudrocks (Pyrenees, northern Spain). *Tectonophysics*, *307*(1), 1–14.
Poblete, F., Roperch, P., Hervé, F., Diraison, M., Espinoza, M., & Arriagada, C. (2014). The curved Magallanes fold and thrust belt: Tectonic insights from a paleomagnetic and anisotropy of magnetic susceptibility study. *Tectonics*, *33*, 2526–2551. https://doi.org/10.1002/2014TC003555
Rees, A. (1965). The use of anisotropy of magnetic susceptibility in the estimation of sedimentary fabric. *Sedimentology*, *4*(4), 257–271.
Robinson, A. C. (2009). Geologic offsets across the northern Karakorum fault: Implications for its role and terrane correlations in the western Himalayan-Tibetan orogen. *Earth and Planetary Science Letters*, *279*(1), 123–130.
Robinson, A. C. (2015). Mesozoic tectonics of the Gondwanan terranes of the Pamir plateau. *Journal of Asian Earth Sciences*, *102*, 170–179.
Robinson, A. C., Yin, A., Manning, C. E., Harrison, T. M., Zhang, S.-H., & Wang, X.-F. (2007). Cenozoic evolution of the eastern Pamir: Implications for strain-accommodation mechanisms at the western end of the Himalayan-Tibetan orogen. *Geological Society of America Bulletin*, *119*(7–8), 882–896.
Robion, P., de Lamotte, D. F., Kissel, C., & Aubourg, C. (1995). Tectonic versus mineralogical contribution to the magnetic fabrics of epi-metamorphic slaty rocks: An example from the Ardennes Massif (France-Belgium). *Journal of Structural Geology*, *17*(8), 1111–1124.
Rohrmann, A., Kapp, P., Carrapa, B., Reiners, P. W., Guynn, J., Ding, L., & Heizler, M. (2012). Thermochronologic evidence for plateau formation in central Tibet by 45 Ma. *Geology*, *40*(2), 187–190.
Roperch, P., Carlotto, V., & Chauvin, A. (2010). Using anisotropy of magnetic susceptibility to better constrain the tilt correction in paleomagnetism: A case study from southern Peru. *Tectonics*, *29*, TC6005. https://doi.org/10.1029/2009TC002639
Roperch, P., Carlotto, V., Ruffet, G., & Fornari, M. (2011). Tectonic rotations and transcurrent deformation south of the Abancay deflection in the Andes of southern Peru. *Tectonics*, *30*, TC2010. https://doi.org/10.1029/2010TC002725
Rutte, D., Ratschbacher, L., Khan, J., Stübner, K., Hacker, B. R., Stearns, M. A., & Sperner, B. (2017). Building the Pamir-Tibet plateau—Crustal stacking, extensional collapse, and lateral extrusion in the central Pamir: 2. Timing and Rates. *Tectonics*, *36*, 385–419. https://doi.org/10.1002/2016TC004294
Rutte, D., Ratschbacher, L., Schneider, S., Stübner, K., Stearns, M. A., Gulzar, M. A., & Hacker, B. R. (2017). Building the Pamir-Tibetan plateau—Crustal stacking, extensional collapse, and lateral extrusion in the central Pamir: 1. Geometry and kinematics. *Tectonics*, *36*, 342–384. https://doi.org/10.1002/2016TC004293
Sagnotti, L., & Winkler, A. (1999). Rock magnetism and palaeomagnetism of greigite-bearing mudstones in the Italian peninsula. *Earth and Planetary Science Letters*, *165*(1), 67–80.
Shanley, K. W., & McCabe, P. J. (1993). Alluvial architecture in a sequence stratigraphic framework: A case history from the Upper Cretaceous of southern Utah, U.S.A. In S. Flint & I. Bryant (Eds.), *Quantitative modeling of clastic hydrocarbon reservoirs and outcrop analoguesInternational Association of Sedimentologists Special Publication* (Vol. 15, pp. 21–55).
Shen, Z. K., Wang, M., Li, Y., Jackson, D. D., Yin, A., Dong, D., & Fang, P. (2001). Crustal deformation along the Altyn Tagh fault system, western China, from GPS. *Journal of Geophysical Research*, *106*(B12), 30,607–30,621.
Sippl, C., Schurr, B., Yuan, X., Mechie, J., Schneider, F. M., Gadoev, M., et al. (2013). Geometry of the Pamir-Hindu Kush intermediate-depth earthquake zone from local seismic data. *Journal of Geophysical Research: Solid Earth*, *118*, 1438–1457. https://doi.org/10.1002/jgrb.50128
Sobel, E. (1995). Basin analysis and apatite fission-track thermochronology of the Jurassic-Paleogene southwest Tarim basin, NW China. (PhD), Stanford University, Stanford.
Sobel, E. R. (1999). Basin analysis of the Jurassic–Lower Cretaceous southwest Tarim basin, northwest China. *Geological Society of America Bulletin*, *111*(5), 709–724. https://doi.org/10.1130/0016-7606(1999)111<0709:baotjl>2.3.co;2
Sobel, E. R., Chen, J., & Heermance, R. V. (2006). Late Oligocene–Early Miocene initiation of shortening in the southwestern Chinese Tian Shan: Implications for Neogene shortening rate variations. *Earth and Planetary Science Letters*, *247*(1–2), 70–81. https://doi.org/10.1016/j.epsl.2006.03.048
Sobel, E. R., Chen, J., Schoenbohm, L. M., Thiede, R., Stockli, D. F., Sudo, M., & Strecker, M. R. (2013). Oceanic-style subduction controls late Cenozoic deformation of the northern Pamir orogen. *Earth and Planetary Science Letters*, *363*, 204–218. https://doi.org/10.1016/j.epsl.2012.12.009

Sobel, E. R., & Dumitru, T. A. (1997). Thrusting and exhumation around the margins of the western Tarim basin during the India-Asia collision. *Journal of Geophysical Research*, *102*(B3), 5043–5063. https://doi.org/10.1029/96JB03267

Sobel, E. R., Schoenbohm, L. M., Chen, J., Thiede, R., Stockli, D. F., Sudo, M., & Strecker, M. R. (2011). Late Miocene–Pliocene deceleration of dextral slip between Pamir and Tarim: Implications for Pamir orogenesis. *Earth and Planetary Science Letters*, *304*(3–4), 369–378. https://doi.org/10.1016/j.epsl.2011.02.012

Soto, R., Larrasoaña, J. C., Arlegui, L. E., Beamud, E., Oliva-Urcia, B., & Simón, J. L. (2009). Reliability of magnetic fabric of weakly deformed mudrocks as a palaeostress indicator in compressive settings. *Journal of Structural Geology*, *31*(5), 512–522.

Staisch, L. M., Niemi, N. A., Clark, M. K., & Chang, H. (2016). Eocene to late Oligocene history of crustal shortening within the Hoh Xil Basin and implications for the uplift history of the northern Tibetan Plateau. *Tectonics*, *35*, 862–895. https://doi.org/10.1002/2015TC003972

Stearns, M., Hacker, B., Ratschbacher, L., Rutte, D., & Kylander-Clark, A. (2015). Titanite petrochronology of the Pamir gneiss domes: Implications for middle to deep crust exhumation and titanite closure to Pb and Zr diffusion. *Tectonics*, *34*, 784–802. https://doi.org/10.1002/2014TC003774

Steckler, M., & Watts, A. (1978). Subsidence of the Atlantic-type continental margin off New York. *Earth and Planetary Science Letters*, *41*(1), 1–13. https://doi.org/10.1016/0012-821X(78)90036-5

Stübner, K., Ratschbacher, L., Rutte, D., Stanek, K., Minaev, V., Wiesinger, M., & Gloaguen, R. (2013). The giant Shakhdara migmatitic gneiss dome, Pamir, India-Asia collision zone: 1. Geometry and kinematics. *Tectonics*, *32*, 948–979. https://doi.org/10.1002/tect.20057

Stübner, K., Ratschbacher, L., Weise, C., Chow, J., Hofmann, J., Khan, J., & Stanek, K. P. (2013). The giant Shakhdara migmatitic gneiss dome, Pamir, India–Asia collision zone, II: Timing of dome formation. *Tectonics*, *32*, 1404–1431. https://doi.org/10.1002/tect.20059

Sun, J., Alloway, B., Fang, X., & Windley, B. F. (2015). Refuting the evidence for an earlier birth of the Taklimakan Desert. *Proceedings of the National Academy of Sciences*, *112*(41), E5556–E5557. https://doi.org/10.1073/pnas.1517525112

Sun, J., & Jiang, M. (2013). Eocene seawater retreat from the southwest Tarim basin and implications for early Cenozoic tectonic evolution in the Pamir plateau. *Tectonophysics*, *588*, 27–38. https://doi.org/10.1016/j.tecto.2012.11.031

Sun, J., & Liu, T. (2006). The age of the Taklimakan Desert. *Science*, *312*(5780), 1621–1621.

Sun, J., Windley, B. F., Zhang, Z., Fu, B., & Li, S. (2016). Diachronous seawater retreat from the southwestern margin of the Tarim basin in the Late Eocene. *Journal of Asian Earth Sciences*, *116*, 222–231. https://doi.org/10.1016/j.jseaes.2015.11.020

Sun, J., Xu, Q., & Huang, B. (2007). Late Cenozoic magnetochronology and paleoenvironmental changes in the northern foreland basin of the Tian Shan Mountains. *Journal of Geophysical Research*, *112*, B04107. https://doi.org/10.1029/2006JB004653

Sun, J., Zhang, Z., & Zhang, L. (2009). New evidence on the age of the Taklimakan Desert. *Geology*, *37*(2), 159–162.

Sun, J., Zhu, R., & Bowler, J. (2004). Timing of the Tianshan Mountains uplift constrained by magnetostratigraphic analysis of molasse deposits. *Earth and Planetary Science Letters*, *219*(3–4), 239–253. https://doi.org/10.1016/S0012-821X(04)00008-1

Tang, T., Yang, H., Lan, X., Yu, C., Xue, Y., Zhang, Y., et al. (1989). *Marine Late Cretaceous and Early Tertiary stratigraphy and petroleum geology in western Tarim basin, China* (pp. 133–140). Beijing: Science Press.

Tarling, D., & Hrouda, F. (1993). *Magnetic anisotropy of rocks*. Suffolk: Chapman and Hall.

Tauxe, L. (1998). Paleomagnetic Procedures. In *Paleomagnetic Principles and Practice. Modern Approaches in Geophysics* (Vol 17, pp. 83–120). Dordrecht: Springer.

Teng, Z., Yue, L., Pu, R., Deng, X., & Bian, X. (1996). The magnetostratigraphic age of the Xiyu formation. *Geological Review*, *42*(6), 481–489.

Thiede, R. C., Sobel, E. R., Chen, J., Schoenbohm, L. M., Stockli, D. F., Sudo, M., & Strecker, M. R. (2013). Late Cenozoic extension and crustal doming in the India-Eurasia collision zone: New thermochronologic constraints from the NE Chinese Pamir. *Tectonics*, *32*, 763–779. https://doi.org/10.1002/tect.20050

Thomas, J., Gapais, D., Cobbold, P., Meyer, V., & Burtman, V. (1996). *Tertiary kinematics of the Tadjik Depression (central Asia): Inferences from fault and fold patterns* (pp. 171–180). Paris: Geodynamic Evolution of Sedimentary Basins. Editions Technip.

Torsvik, T. H., Van der Voo, R., Preeden, U., Mac Niocaill, C., Steinberger, B., Doubrovine, P. V., & Tohver, E. (2012). Phanerozoic polar wander, palaeogeography and dynamics. *Earth-Science Reviews*, *114*(3–4), 325–368.

Van Hinsbergen, D. J., Kapp, P., Dupont-Nivet, G., Lippert, P. C., DeCelles, P. G., & Torsvik, T. H. (2011). Restoration of Cenozoic deformation in Asia and the size of Greater India. *Tectonics*, *30*, TC5003. https://doi.org/10.1029/2011TC002908

Van Hinte, J. (1978). Geohistory analysis—Application of micropaleontology in exploration geology. *AAPG Bulletin*, *62*(2), 201–222.

Vandamme, D. (1994). A new method to determine paleosecular variation. *Physics of the Earth and Planetary Interiors*, *85*, 131–142.

Wang, C., Zhao, X., Liu, Z., Lippert, P. C., Graham, S. A., Coe, R. S., & Li, Y. (2008). Constraints on the early uplift history of the Tibetan plateau. *Proceedings of the National Academy of Sciences*, *105*(13), 4987–4992.

Wang, S., & Peng, S. (2013). *Regional geological survey reports People's Republic of China, 1: 250.000 Yecheng pieces J43C003004*, (Chinese ed. p. 183). Beijing: Chinese Geology University Press.

Wang, Z., & Wang, X. (2016). Late Cenozoic deformation sequence of a thrust system along the eastern margin of Pamir, northwest China. *Acta Geologica Sinica (English Edition)*, *90*(5), 1664–1678.

Wei, H.-H., Meng, Q.-R., Ding, L., & Li, Z.-Y. (2013). Tertiary evolution of the western Tarim basin, northwest China: A tectono-sedimentary response to northward indentation of the Pamir salient. *Tectonics*, *32*, 558–575. https://doi.org/10.1002/tect.20046

Wei, X., Zheng, H., Wang, P., Tada, R., Clift, P. D., Jourdan, F., et al. (2018). Miocene volcaniclastic sequence within the Xiyu formation from source to sink: Implications for drainage development and tectonic evolution in eastern Pamir, NW Tibetan plateau. *Tectonics*, *37*, 3261–3284. https://doi.org/10.1029/2018TC005008

Yang, W., Dupont-Nivet, G., Jolivet, M., Guo, Z., Bougeois, L., Bosboom, R., & Heilbronn, G. (2015). Magnetostratigraphic record of the early evolution of the southwestern Tian Shan foreland basin (Ulugqat area), interactions with Pamir indentation and India–Asia collision. *Tectonophysics*, *644*, 122–137.

Yang, W., Jolivet, M., Dupont-Nivet, G., & Guo, Z. (2014). Mesozoic–Cenozoic tectonic evolution of southwestern Tian Shan: Evidence from detrital zircon U/Pb and apatite fission track ages of the Ulugqat area, northwest China. *Gondwana Research*, *26*(3), 986–1008.

Yin, A., & Harrison, T. M. (2000). Geologic evolution of the Himalayan-Tibetan orogen. *Annual Review of Earth and Planetary Sciences*, *28*(1), 211–280.

Yin, A., Rumelhart, P., Butler, R. E., Cowgill, E., Harrison, T. M., Foster, D. A., & Raza, A. (2002). Tectonic history of the Altyn Tagh fault system in the northern Tibet inferred from Cenozoic sedimentation. *Geological Society of America Bulletin*, *114*(10), 1257–1295.

Zhao, H., Wei, Y., Shen, Y., Xiao, A., Mao, L., Wang, L., & Wu, L. (2016). Cenozoic tilting history of the south slope of the Altyn Tagh as revealed by seismic profiling: Implications for the kinematics of the Altyn Tagh fault bounding the northern margin of the Tibetan Plateau. *Geosphere*, *12*(3), 884–899.

Zheng, H., Huang, X., & Butcher, K. (2006). Lithostratigraphy, petrography and facies analysis of the Late Cenozoic sediments in the foreland basin of the west Kunlun. *Palaeogeography, Palaeoclimatology, Palaeoecology*, *241*(1), 61–78. https://doi.org/10.1016/j.palaeo.2006.06.015

Zheng, H., Powell, C. M., An, Z., Zhou, J., & Dong, G. (2000). Pliocene uplift of the northern Tibetan plateau. *Geology*, *28*(8), 715–718.

Zheng, H., Tada, R., Jia, J., Lawrence, C., & Wang, K. (2010). Cenozoic sediments in the southern Tarim basin: Implications for the uplift of northern Tibet and evolution of the Taklimakan Desert. *Geological Society, London, Special Publications*, *342*(1), 67–78. https://doi.org/10.1144/sp342.6

Zheng, H., Wei, X., Tada, R., Clift, P. D., Wang, B., Jourdan, F., & He, M. (2015a). Late Oligocene–Early Miocene birth of the Taklimakan Desert. *Proceedings of the National Academy of Sciences*, *112*(25), 7662–7667. https://doi.org/10.1073/pnas.1424487112

Zheng, H., Wei, X., Tada, R., Clift, P. D., Wang, B., Jourdan, F., & He, M. (2015b). Reply to Sun et al.: Confirming the evidence for Late Oligocene–Early Miocene birth of the Taklimakan Desert. *Proceedings of the National Academy of Sciences*, *112*(41), E5558–E5559.

Zhou, Z. Y. (2000). *Stratigraphy of the Tarim basin*. Beijing: Beijing Science Press.

Zubovich, A., Schöne, T., Metzger, S., Mosienko, O., Mukhamediev, S., Sharshebaev, A., & Zech, C. (2016). Tectonic interaction between the Pamir and Tien Shan observed by GPS. *Tectonics*, *35*, 283–292. https://doi.org/10.1002/2015TC004055